

Determination of the optimal camera distance for cloud height measurements with two all-sky imagers

P. Kuhn^{1,*}

German Aerospace Center (DLR), Institute of Solar Research, Ctra. de Senés s/n km 4, 04200 Tabernas, Spain.

B. Nouri¹, S. Wilbert¹, N. Hanrieder¹, C. Prahl¹, L. Ramirez², L. Zarzalejo², T. Schmidt³, T. Schmidt⁴, Z. Yasser⁵, D. Heinemann³, P. Tzoumanikas⁶, A. Kazantzidis⁶, J. Kleissl⁷, P. Blanc⁸, R. Pitz-Paal⁹

Abstract

All-sky imager based systems can be used to measure a number of cloud properties. Configurations consisting of two all-sky imagers can be used to derive cloud heights for weather stations, aviation and nowcasting of solar irradiance. One key question for such systems is the optimal distance between the all-sky imagers. This problem has not been studied conclusively in the literature. To the best of our knowledge, no previous in-field study of the optimal camera distance was performed. Also, comprehensive modeling is lacking.

Here, we address this question with an in-field study on 93 days using 7 camera distances between 494 m and 2562 m and one specific cloud height estimation approach. We model the findings and draw conclusions for various configurations with different algorithmic methods and camera hardware.

The camera distance is found to have a major impact on the accuracy of cloud height determinations. For the used 3 megapixel cameras, cloud heights up to 12000 m and the used algorithmic approaches, an optimal camera distance of approximately 1500 m is determined. Optimal camera distances can be reduced to less than 1000 m if higher camera resolutions (e.g. 6 megapixel) are deployed. A step-by-step guide to determine the optimal camera distance is provided.

Keywords: All-sky imagers, cloud height measurements, solar nowcasting

*Corresponding author

Email address: Pascal.Kuhn@dlr.de (P. Kuhn)

¹German Aerospace Center (DLR), Institute of Solar Research, Ctra. de Senés s/n km 4, 04200 Tabernas, Spain.

²CIEMAT, Energy Department - Renewable Energy Division. Av. Complutense, 40, 28040 Madrid, Spain.

³German Aerospace Center (DLR), Institute of Networked Energy Systems, Carl-von-Ossietzky-Straße 15, 26129 Oldenburg, Germany.

⁴CSP Services GmbH, Friedrich-Ebert-Ufer 30, 51143 Cologne, Germany.

⁵TSK FLAGSOL, Cologne, Anna-Schneider-Steig 10, 50678 Cologne, Germany.

⁶Laboratory of Atmospheric Physics, Department of Physics, University of Patras, 26500 Patras, Greece.

⁷Dept. of Mechanical and Aerospace Engineering, UCSD Center for Energy Research, University of California, 92093-0411 La Jolla, USA.

⁸MINES ParisTech, PSL Research University, Centre Observation, Impacts, Energy (O. I. E.), CS 10207, F-06904, Sophia Antipolis CEDEX, France.

⁹German Aerospace Center (DLR), Institute of Solar Research, Linder Höhe, 51147 Cologne, Germany.

1. Introduction

Cloud heights are of interest for energy meteorological applications such as the nowcasting of solar irradiance (Nouri et al. (2017), Chu et al. (2017)), weather services (e.g. Campbell et al. (2018), Müller et al. (2018)) and aviation (Wiegmann et al. (2002), Mecikalski et al. (2007)), where cloud height is critical for non-instrument flight operations. All-sky imager based systems can provide such cloud height measurements. In comparison to ceilometers, they are less expensive, can provide multiple cloud heights at once and are not confined to a point-like measurement area above the instrument. In recent years, many approaches to determine cloud heights based on two (or more) all-sky imagers were published (see Tab. 1).

Due to the low installation and maintenance costs, all-sky imager configurations with two cameras are especially relevant. Moreover, in Kuhn et al. (2018b), such a configuration is found to be the most promising one out of five different cloud height providing systems. A key question for such systems is the optimal distance between the cameras. This question is addressed here. The answer to that question depends on a multitude of chosen hardware and software parameters.

To the best of our knowledge, the question of the optimal camera distance was not previously investigated with in-field studies. This might have been caused by the uncertainty achieved using all-sky imagers for cloud height estimations being considered too high for certain applications. Recently, however, mean absolute deviations of 17 % were reported (Nouri et al., 2018b), demonstrating the potential of such approaches.

In most publications listed in Tab. 1, the used camera distance is not specifically motivated or studied, but seems to be imposed by local availability. In the following, we briefly summarize previous works relevant for this study.

Using cameras with a similar resolution (1748×1748 pixels) as the cameras used here and a distance of 1230 m, Nguyen and Kleissl (2014) derive that clouds at 2627 m can be optimally measured and the configuration is reliable up to 5250 m. These values are derived by looking at the change of the overlap between the cameras' viewing cones ($\Delta\text{Overlap}$, change in the sky area seen by both cameras) in relation to the change in cloud height. A threshold of $\frac{\Delta\text{Overlap}}{\Delta\text{cloud base height}} = \frac{0.1\%}{100\text{ m}}$ is chosen for "*demonstration purposes*" and not further motivated. The dependency on the camera resolution is not studied. However, the interplay between cloud heights and the optimal camera distance is identified.

In Massip et al. (2015), a stereographic sensitivity [pixel/m] study is conducted for four of the five cameras used here, including a study on the directional dependencies on a 4 km² area and a cloud base height of 3000 m. The stereographic sensitivity can be derived from the camera resolution and the parallax in pixel caused by an altitude variation of the cloud height in [m]. "*For limited variation of altitude (less than 500 m), this stereoscopic sensitivity is linearly increasing*" with decreasing cloud height. A direct translation of these findings into an optimal camera distance is difficult. However, Massip

Table 1: Camera distances and resolutions used for cloud height measurements as published in literature.

Reference	Camera distance	Camera resolution
de WA (1885)	410 m	theodolites (human eye)
Strachey and Whipple (1891)	730 m	analog camera
Kassander and Sims (1957)	2100 m	analog camera
Orville and Jr. (1961)	4820 m	analog camera
Allmen and Kegelmeyer Jr (1996)	5540 m	256×256 pixels (indicated in Johnson et al. (1989))
Kassianov et al. (2005)	540 m	352×288 pixels
Seiz et al. (2007)	850 m	3060×2036 pixels / 3072×2048 pixels
Damiani et al. (2008)	not specified	2048×1536 pixels
Hu et al. (2009)	1500 m	2048×1536 pixels
Janeiro et al. (2012)	28.9 m	3888×2592 pixels
Urquhart et al. (2012)	1800 m	640×480 pixels
Nguyen and Kleissl (2014)	1230 m	1750×1750 pixels
Öktem et al. (2014)	1000 m	1296×960 pixels / 1024×768 pixels
Andreev et al. (2014)	17 m	3072×2304 pixels
Peng et al. (2015)	2477 m / 956 m	640×480 pixels
Roy (2016)	590 m	2560×1920 pixels
Beekmans et al. (2016)	300 m	2448×2048 pixels
Katai-Urban et al. (2016)	90 m	5184×3456 pixels
Savoy et al. (2017)	100 m	5184×3456 pixels
Blanc et al. (2017)	572 m	2048×1536 pixels
Katai-Urban et al. (2018)	90/100/130 m	5184×3456 pixels

36 et al. (2015) highlight the anisotropy and sensitivity of cloud height measurements, raising the related
37 question of the best orientation of a two camera system for given local conditions such as prevailing wind
38 direction. This question is briefly addressed in section 5.

39 Katai-Urban et al. (2018) model the challenges of camera-based cloud height derivations and address
40 the question of the optimal camera distance for cloud heights between 1000 m and 2000 m. They find
41 that for the applied approaches, using a camera resolution of 5184×3456 pixels, cloud height deviations
42 decrease up to a camera distance of 200 m. Beyond a camera distance of 200 m, little improvements are
43 found. Without further explanations, optimal camera distances between 2000 m and 10000 m for cloud
44 heights between 1000 m and 5000 m are postulated in Katai-Urban et al. (2016), also stating that such
45 large distance would *"show too much geometric and photometric distortion, which makes the matching*
46 *of cloud pixels unfeasible"* (Katai-Urban et al. (2016)).

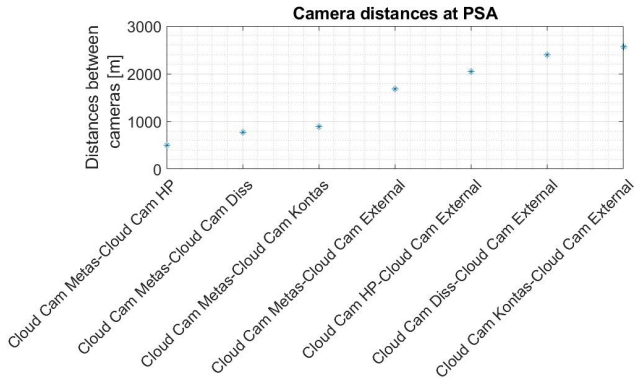
47 Our approach to address the question of the optimal camera distance for cloud height measurements
48 with two all-sky imagers is twofold:

49 (1) We present an in-field study with various camera distances within a two camera configuration
50 (section 2). In this study, cloud heights derived from configurations with different camera distances are
51 compared to cloud base heights measured by a ceilometer. (2) In a second step, we model the expected
52 cloud height deviations as a function of the camera distance to determine the optimal distance and
53 compare the results to the finding of the field study (section 3).

54 Usually, camera-based cloud height measurements approaches rely on cloud segmentation or locating
55 common points of interest within images, which might be, according to Bernecker et al. (2013), a main
56 origin of errors. To reduce hardware dependencies and increase the robustness, a cloud segmentation-
57 independent approach to derive cloud heights from two all-sky imagers is developed in Kuhn et al.
58 (2018b). This approach is explained in the next section and used here.

59 In section 4, we attempt to extrapolate the findings to different camera hardware. The distances
60 between the cameras are not only relevant for the accuracy of cloud height measurements, but also
61 for other aspects. For instance, large distances between cameras lead to a larger area of the sky being
62 imaged by the multi-camera system. Such considerations will be discussed in section 5. The applicability
63 of the findings to other all-sky imager based cloud height estimation algorithms is studied in section 6.
64 A step-by-step guide to define relevant parameters is included in section 7. The conclusion is given in
65 section 8. This study is motivated by the industrial and practical relevance as well as by the variety of
66 different camera distances used in the literature (see Tab. 1).

67 To summarize our findings, a list of parameters that impact the optimal camera distance is given
68 here in decreasing importance: (1) cloud height itself, (2) camera resolution, (3) minimum viewing angle,
69 (4) cloud positions in relation to the image geometry and (5) cloud positions in relation to the cameras'
70 axis.



(a) Camera distances at PSA.



(b) Cameras' positions at PSA: White x mark the cameras' positions and the black star marks the position of the ceilometer. [googlemaps]

Figure 1: Cameras' positions and distances at the Plataforma Solar de Almería (PSA).

71 **2. In-field study of cloud heights derived by two all-sky imagers at different camera dis-**
 72 **tances**

73 *2.1. Approach, settings and configurations*

74 This study is conducted using five all-sky imagers and seven camera distances on the Plataforma
 75 Solar de Almería (PSA) in southern Spain. The positions of the cameras are indicated in Fig. 1. The
 76 minimum distance is 494 m, the maximum distance is 2562 m. Although there is a gap between 890 m
 77 and 1679 m, the distances are well distributed and, as of 2018, globally unique for such a study (see
 78 Fig. 1). The all-sky imagers have a resolution of 3 megapixel (MP) and are off-the-shelf surveillance
 79 cameras (Mobotix, Q24 at Metas, HP and Diss as well as Q25 at Kontas and External. All cameras use
 80 CMOS chips.).

81 Pairs of two cameras are used to calculate the cloud height as described in, benchmarked on 59 days
 82 against four other systems in and with the same parameters of Kuhn et al. (2018b). This approach is
 83 briefly summarized here and shown in Fig. 2. To derive a cloud height, two images from both cameras,
 84 taken 30 s apart, are subtracted ($d_i(x, y)$ in Fig. 2) and projected into one orthoimage for each camera
 85 ($o_i(m, n)$). These difference orthoimages are segmented into binary images ($b_i(m, n)$) by using a dynamic
 86 threshold (98th percentile). The binary images are then matched, deriving a cloud speed in [pixel/s].
 87 This so-called *matching distance* between the orthoimages is a key parameter and corresponds to the
 88 known distance of the camera. This allows the conversion of the matching distance from [pixel/s] to [m/s].
 89 With both the angular and the absolute velocity derived, one general cloud height for each timestamp
 90 is calculated for the whole image.

91 This approach is independent from cloud detection algorithms, which reduces dependencies on camera
 92 hardware. For instance, different camera chip models are used in this study. The novel differential

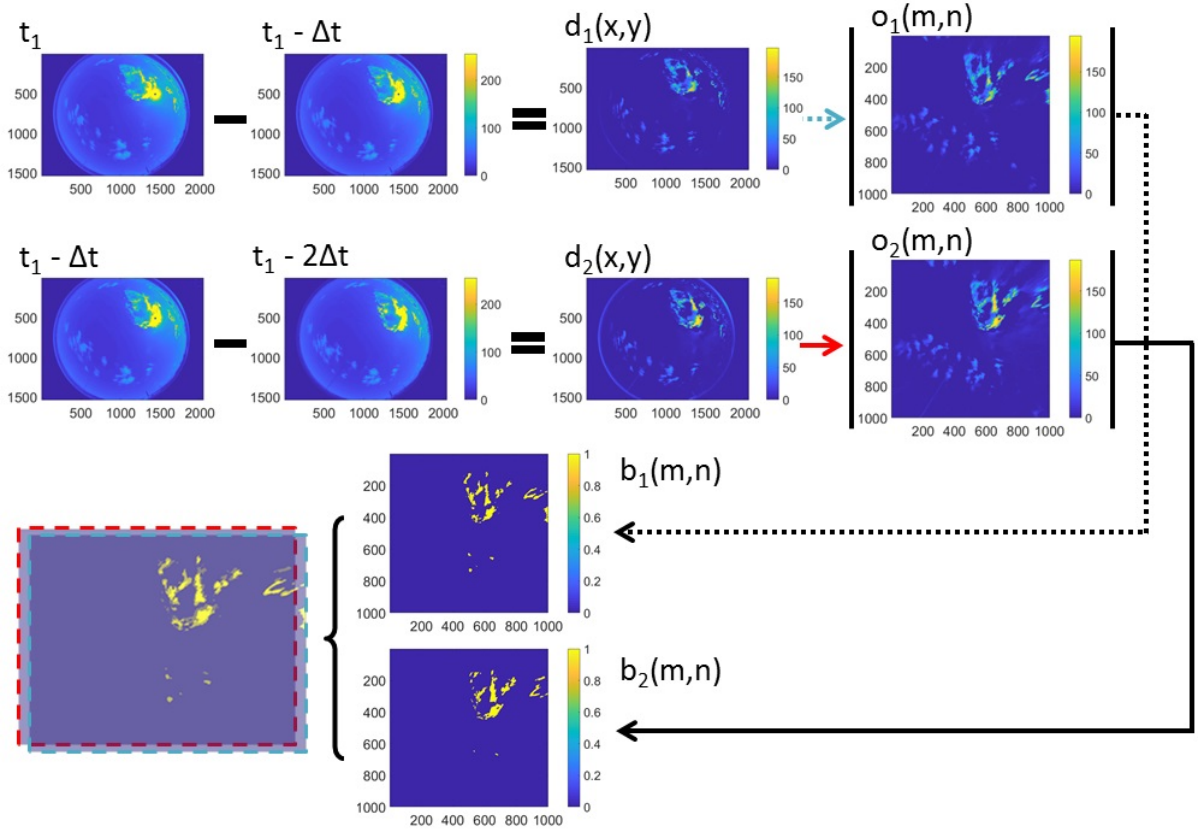


Figure 2: Working principle of the cloud height derivation using two all-sky imagers (adapted from Kuhn et al. (2018b)).

93 approach matches cloud velocities, not specific points of interests within all-sky images. In a fisheye
 94 image, this (angular) velocity depends on the position of the cloud within the image. This effect is
 95 corrected by transforming the fisheye image into an orthoimage. If the same cloud is seen by both all-
 96 sky imagers, matching its velocity is considered far more robust than matching points of interest, which
 97 might also be more challenging due to perspective differences. As a result of the dynamic threshold, cloud
 98 speeds and heights are also derived during overcast situations for which approaches based on matching
 99 segmented binary cloud masks cannot provide measurements. The algorithm used in this study provides
 100 one cloud height for each pair of all-sky images. However, in Nouri et al. (2018b), this differential
 101 approach for cloud height estimation was expanded to provide several cloud heights. If multiple cloud
 102 heights are measured simultaneously, matching these measurements to ceilometer data becomes more
 103 complicated. As the focus of this study is on the optimal camera distance, these challenges are avoided
 104 by using one cloud height per timestamp on a dataset filtered for constant cloud height situations (see
 105 explanations below).

106 Here, as inputs, jpg images are used, whose color channel values (1) have suffered a lossy discrete
 107 cosine transformation and (2) are confined to discrete values between 0 and 255. However, jpg images are

108 considered to be feasible as the amount of data is far smaller than e.g. while using tiff images, the lossy
 109 compression does not introduce strong blurring effects and the discretization was found to be irrelevant
 110 with usual pixel values beyond 100 at the cloud edges in the difference images.

111 Although independent from cloud segmentation algorithms, the exterior and internal orientations of
 112 the cameras must be known to calculate the orthoimages. The used orthoimages have a resolution of
 113 1000×1000 pixels ($N \times N$). In principle, this resolution could be increased. However, due to the limited
 114 amount of pixels on the cameras' chips, this increase would not yield more physical information. The
 115 minimum elevation angle $\alpha = 12^\circ$ is the minimum angle present in the orthoimage for all azimuth angles.
 116 In the edges of the quadratic orthoimage, smaller elevation angles are projected into the orthoimage,
 which is considered to be of minor importance in this study. Figure 3 visualizes these parameters.

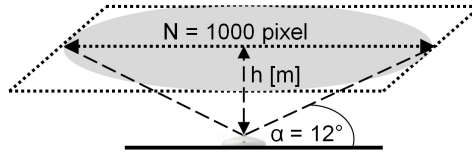


Figure 3: Sketch showing the properties of the orthoimage (adapted from Kuhn et al. (2018b)).

117

118 Conventional deviation metrics such as root-mean-square deviations (RMSD), standard deviation
 119 (std), mean-absolute deviations (MAD) and bias (equ. 1-4) on 10 min gliding medians are used to
 120 quantify the deviations between the all-sky imager derived cloud heights ($h_{\text{ASI-ASI},i}$) and the ceilometer
 121 cloud base heights ($h_{\text{ceilometer},i}$).

$$122 \quad \text{bias} = \frac{1}{N} \sum_{i=1}^N (h_{\text{ASI-ASI},i} - h_{\text{ceilometer},i}) \quad (1)$$

$$123 \quad \text{std} = \sqrt{\frac{1}{N} \sum_{i=1}^N ((h_{\text{ASI-ASI},i} - h_{\text{ceilometer},i}) - \text{bias})^2} \quad (2)$$

$$124 \quad \text{RMSD} = \sqrt{\frac{1}{N} \sum_{i=1}^N (h_{\text{ASI-ASI},i} - h_{\text{ceilometer},i})^2} \quad (3)$$

$$125 \quad \text{MAD} = \frac{1}{N} \sum_{i=1}^N |h_{\text{ASI-ASI},i} - h_{\text{ceilometer},i}| \quad (4)$$

126 Cloud heights as measured by the ceilometer and the cloud heights measured by the all-sky imager
 127 systems are not identical: Ceilometers measure cloud base heights directly above the position of the
 128 instrument. On the other hand, the all-sky imager based approach used here is more likely to measure
 129 a mean cloud height of optically thick clouds. Also, ceilometers can show "a considerable degree of
 130 scatter" (Martucci et al., 2010) and comparisons found an average bias of 160 m (Martucci et al., 2010)

131 or 50 m (Gaumet et al., 1998) between two ceilometers. Nonetheless, we consider the ceilometer used
 132 here (CHM 15k NIMBUS, G. Lufft Mess- und Regeltechnik GmbH) to be a valid reference.

133 The evaluation is conducted for periods during which the ceilometer measured a temporally relatively
 134 constant cloud height. This limitation is needed to avoid multiple cloud height situations. These situa-
 135 tions are excluded as the ceilometer conducts point-like measurements whereas the all-sky imager systems
 136 determine the heights of clouds causing the largest difference in the difference images (see Fig. 2). In sit-
 137 uations, in which both optically thick cumulus clouds and optically thin ice clouds are present, the all-sky
 138 imager configurations thus tend to derive the height of the (usually lower) cumulus clouds. Therefore,
 139 in multi-layer conditions, systematic deviations between the camera-derived and the ceilometer mea-
 140 surements are present, which are not the subject of this study. Thus, multi-layer cloud situations are
 141 excluded.

142 The periods of temporally relatively constant cloud heights are manually pre-selected by looking for
 143 constant cloud height conditions in ceilometer measurements. In a second step, timestamps for which
 144 the ceilometer measures a standard deviation in cloud base heights larger than 30 % relative to the
 145 ceilometer mean cloud base height measurements within a period of 3 h (90 min around each timestamp)
 146 are excluded. Moreover, only timestamps for which all systems derived a cloud height are included in
 147 the comparison. This leads to a total of 39491 timestamps on 93 days.

148 *2.2. Experimental results of the in-field study on cloud heights using different camera distances*

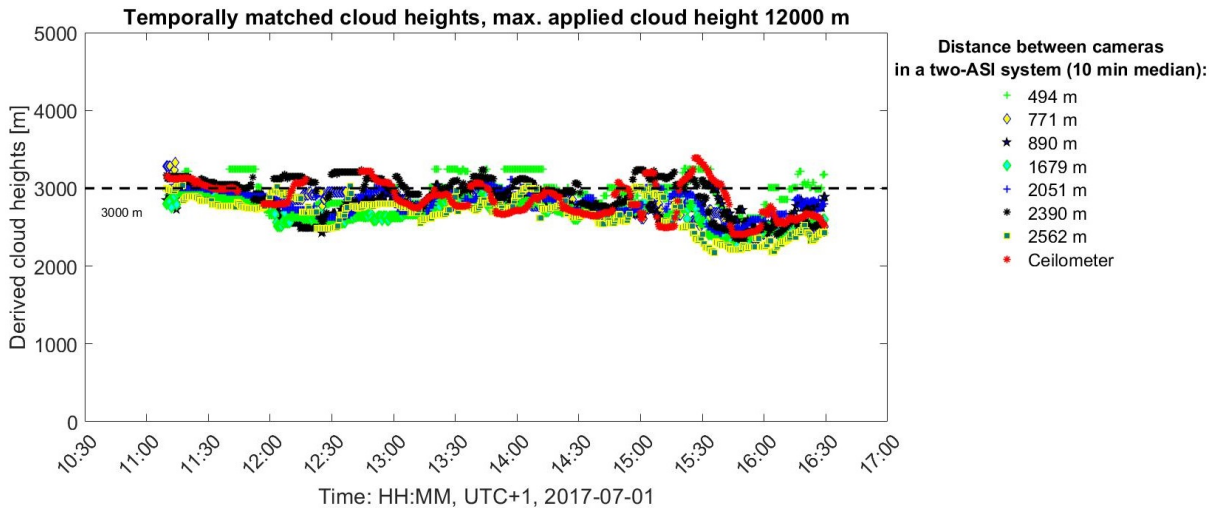


Figure 4: Raw data of all-sky imager derived cloud heights in comparison to ceilometer cloud base heights on 2017-07-01.

149 We specifically look at the raw data of three of the 93 days to highlight certain effects. The first
 150 day, 2017-07-01, is shown in Fig. 4. Throughout the selected period of time, a constant cloud height of
 151 3000 m is present, which is accurately measured by all configurations. On 2017-01-19, shown in Fig. 5,

152 the ceilometer also measures a relatively constant cloud height at about 2000 m. However, configurations
 153 with large camera distances show significant deviations.

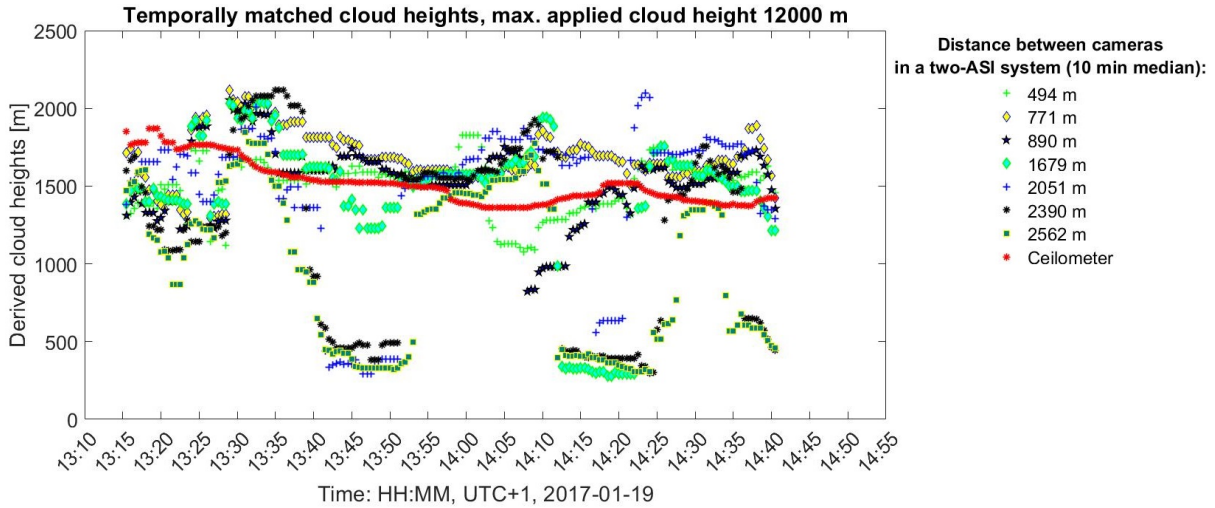


Figure 5: Raw data of all-sky imager derived cloud heights in comparison to ceilometer cloud base heights on 2017-01-19.

153

154 Figure 6 depicts the cloud heights measured during a selected period on 2017-05-29. During that
 155 period, the ceilometer measures a constant cloud height at about 7000 m. Configurations with small
 156 camera distances of 494 m and 890 m often over-estimate this cloud height, with overshootings being
 157 present especially for the setup with the smallest distance. The configuration with the camera distance
 158 of 771 m, however, does not show such overshootings.

159 Larger camera distances of 1679 m, 2051 m, 2390 m and 2562 m derive cloud heights similar to
 160 the ceilometer cloud heights between 17:00 h and 17:50 h. Between 16:20 h and 16:45 h, these setups
 161 measure lower cloud heights than the ceilometer. During this period, high ice clouds are present over
 162 the ceilometer. The all-sky imager, however, also image lower cumulus clouds (see Fig. 7). Due to the
 163 differential approach of the all-sky imager setups, such cumulus clouds are more likely to be matched as
 164 optically thin ice clouds. Therefore, the all-sky imager derived cloud heights of approximately 2000 m
 165 might be physically correct. The step increase in the estimated cloud heights visible in Fig. 6 at
 166 approximately 16:50 h is caused by the 10 min gliding median applied to the all-sky imager measurements.

167

168 For the following comparisons, cloud heights are called "low" if the ceilometer measures a height at
 169 or below 3000 m. "High" cloud heights correspond to ceilometer measurements at or above 8000 m.
 170 "Medium" cloud heights correspond to ceilometer measurements between 3000 m and 8000 m.

171 All-sky imager derived cloud heights above 12,000 m are set to this maximum cloud height. The
 172 applied maximum cloud height is introduced to physically limit the all-sky imager derived cloud heights
 173 and does not affect ceilometer measurements.

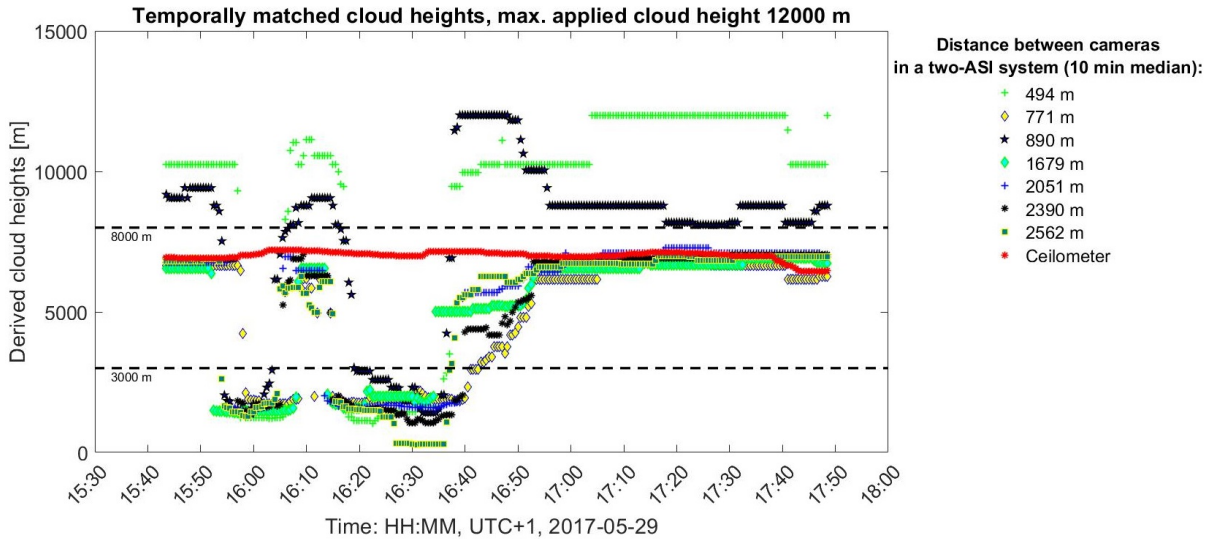


Figure 6: Raw data of all-sky imager derived cloud heights in comparison to ceilometer cloud base heights on 2017-05-29.

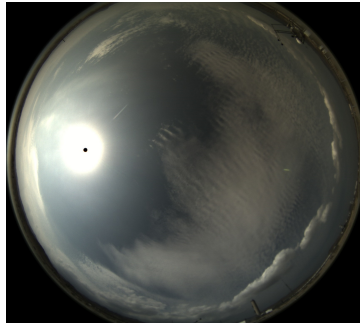


Figure 7: Fisheye all-sky image taken by the Metas camera on 2017-05-29 16:45:00 UTC+1. Both high clouds (image center) and lower clouds (e.g. bottom right edge) are visible. The ceilometer measures base heights of clouds visible in the center of this image.

174 The deviations are displayed in Fig. 8 for low, medium and high clouds as well as all considered
 175 camera distances. The number of measurements used in this comparison for all system is 18927 for low
 176 clouds, 14935 for medium clouds and 5629 for high clouds.

177 For high clouds (dotted lines), the deviations decrease with larger camera distances: From 98.8 %
 178 RMSD for the smallest camera distance (494 m) via 60.3 % at a distance of 1679 m to 62.7 % for the
 179 maximum distance considered here (2562 m) The same holds, on a lower deviation level, for medium
 180 clouds (dashed lines, from 64.8 % RMSD via 21.2 % to 29.2 %). For low clouds (solid lines), the deviations
 181 increase with larger camera distances (from 11.4 % RMSD via 12.0 % to 22.4 %).

182 For high clouds, the second smallest distance (771 m) sticks out with a significant negative bias. This
 183 bias is not present for this distance for low and medium clouds, for which this distance is more accurate
 184 than similar distances.

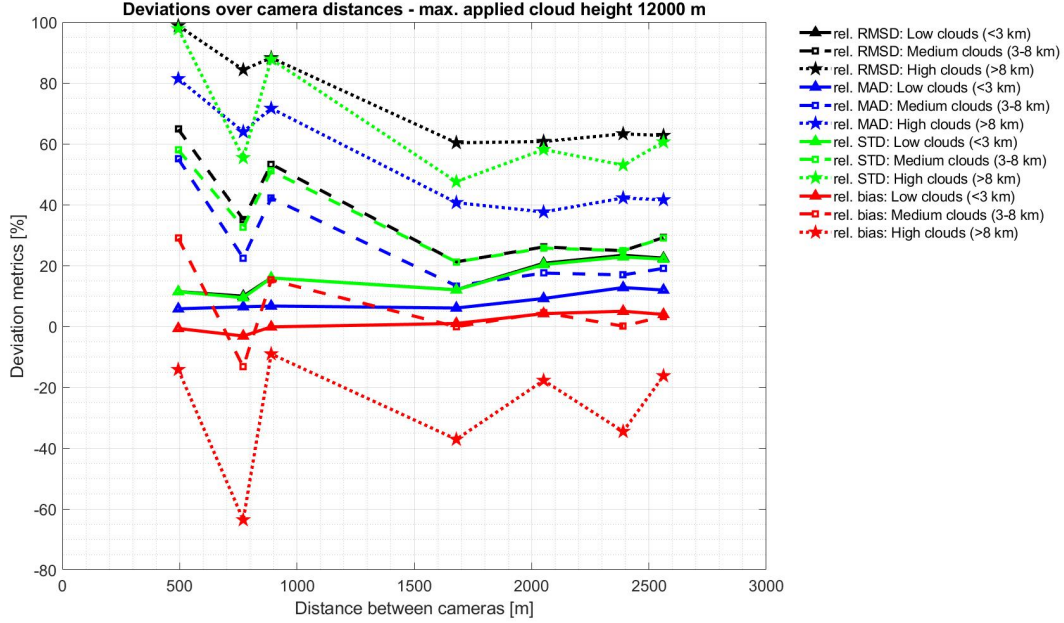


Figure 8: Derived cloud height deviations on 93 days using 7 camera distances. The number of measurements for low clouds is 18927, for medium clouds 14935 and for high clouds 5629.

185 The MADs and the standard deviations show trends similar to those of the RMSD with a tendency
186 to decrease for larger camera distances and high clouds as well as to increase for larger camera distances
187 and low clouds. For high clouds, the MAD decreases from 81.4 % (494 m) to 37.6 % (2051 m) and 41.6 %
188 (2562 m). For medium clouds, the MAD decreases from 55.1 % (494 m) to 19.1 % (2562 m). For low
189 clouds, the MAD increases from 5.8 % (494 m) to 11.9 % (2562 m).

190 The standard deviation drops for high clouds from 97.8 % (494 m) to 60.6 % (2562 m) with a minimum
191 of 47.6 % for a camera distance of 1679 m. For medium cloud heights, the standard deviation decreases
192 from 58.0 % (494 m) to 29.0 % (2562 m) with a minimum of 21.2 % for 1679 m. For low clouds, the
193 standard deviation increases from 11.4 % (494 m) via 9.4 % (771 m) and 22.8 % (2390 m) to 22.1 %
194 (2562 m).

195 In Fig. 8, we see two distinct trends: (1) For medium and high clouds, the deviations shrink with
196 larger camera distances up to 1679 m. For camera distances beyond 1679 m, no major improvements of
197 the metrics are found. (2) For low clouds, the deviations increase with larger camera distances.

198 To further study the impact of different camera distances, scatter density plots of each configuration
199 are shown in Fig. 9a-9g. The scatter density plots visualize the cloud height deviations found between
200 the all-sky imager configuration and the reference ceilometer.

201 Fig. 9a shows the scatter density plot for the smallest camera distance (494 m). This configuration
202 is able to accurately derive cloud heights up to approximately 2500 m. Greater cloud altitudes are

203 measured with a significant amount of scatter. Many clouds, measured by the ceilometer to have heights
204 between 11000 m and 12000 m, are determined by this configuration to have heights of about 2000 m.
205 This could be an indication that not every multi-layer cloud situation is filtered out. As the filtering
206 is only conducted on the data of the ceilometer reference, clouds not being measured by the ceilometer
207 could cause this effect. In such situations, the ceilometer might determine the altitude of a high cloud
208 directly above the instrument whereas the all-sky imager system may measure a general height of other
209 clouds in the sky. As highlighted with Fig. 7, this could explain a certain amount of the artefacts seen
210 in the scatter density plots (Fig. 9a-9g).

211 In Fig. 9b, the scatter density plot corresponding to a camera distance of 771 m is presented. This
212 system measures cloud heights up to approximately 3000 m with better accuracy for cloud heights
213 between 3000 m and 5000 m compared to the 494 m system. The scatter at higher altitudes is biased,
214 meaning that the system underestimates cloud heights more frequently than overestimations occur. This
215 is reflected in the large negative bias shown in Fig. 8.

216 The configuration with a camera distance of 890 m is depicted in Fig. 9c. In contrast to the very
217 similar distance of 771 m, shown in Fig. 9b, the scatter is not biased towards lower estimations. However,
218 for cloud heights above 2500 m, cloud heights cannot be accurately determined. Fig. 9d shows the
219 configuration with the overall best accuracy, having a camera distance of 1679 m. Low, medium and high
220 cloud heights are derived with less scatter in comparison to other distances. For larger camera distances
221 (Fig. 9e-9g), the scatter increases in comparison to the results of the camera distance of 1679 m.

222 Figure 10 shows the standard deviations of the configurations relative to ceilometer cloud base heights
223 for a bin size of 200 m. Corresponding to Fig. 8 and 9, we see that small camera distances (solid lines)
224 scatter less than large camera distance (dotted lines) for low cloud heights, but scatter more for high
225 clouds. Beyond 10000 m, the scatter is similar for all camera distances, which is contributed to the
226 discussed multi-layer situations.

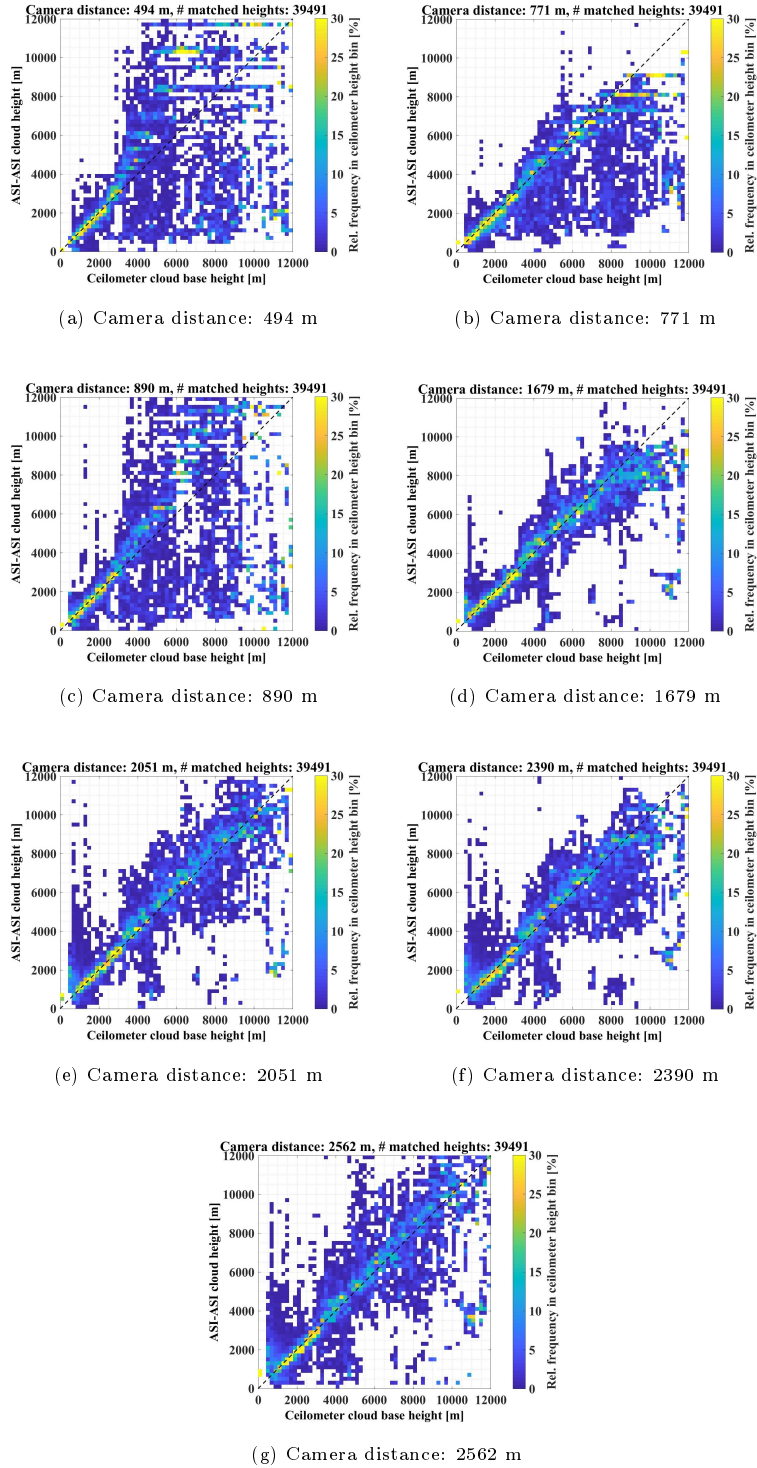


Figure 9: Scatter density plot for cloud heights on 93 days derived by two all-sky imagers and various camera distances. Cloud heights derived from both the all-sky imagers and the ceilometer are compared with a bin size of 200 m. The color shows the relative frequency of the temporally matched cloud heights within each ceilometer cloud height bin. This means that the relative frequencies in one column, which is one ceilometer cloud height bin, add up to 100 %. The results are displayed again for 10 minute medians derived from the all-sky imager systems and compared to 10-minute median measurements of the ceilometers.

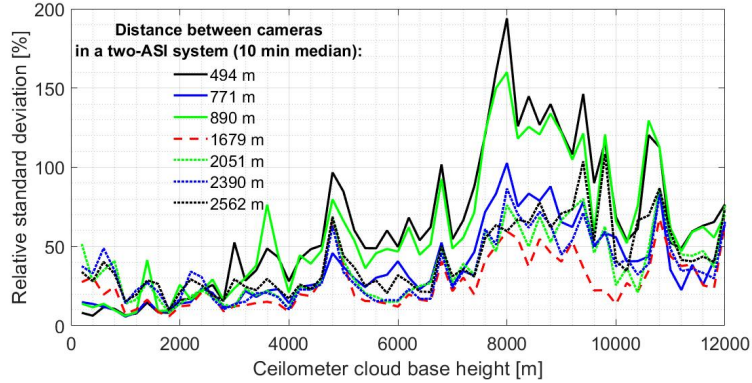


Figure 10: Standard deviation relative to ceilometer cloud base height for all considered all-sky imager systems (bin size: 200 m).

227 3. Modeling the findings of the in-field study

228 3.1. Explaining deviations for small distances and high clouds

229 In order to study the overshooting effects visible e.g. in Fig. 6 and Fig. 9a for small camera distances
 230 and high clouds, we study a specific timestamp. This timestamp is 2017-08-04, 13:47:00 UTC+1. For
 231 this timestamp, the ceilometer measures a cloud height of 11613 m. The two all-sky imager system with
 232 a camera distance of 1678 m derives a cloud height of 10353 m, the system with 494 m camera distance
 233 calculates a non-physical cloud height of 53066 m (53 km). The derived cloud velocity [pixel/s] of both
 234 systems is the same: $\Delta y = 0$ pixel/30 s and $\Delta x = -1$ pixel/30 s. The same velocity in [pixel/s] derived
 235 from $d_1(x, y)$ and $d_2(x, y)$ in Fig. 2 leads, due to the different camera distances, to distinctly different
 236 cloud velocities of 3.2 m/s (for a camera distance of 1678 m) and 16.4 m/s (for the camera distance of
 237 494 m) and hence to the high deviation in the derived cloud heights (10353 m and 53066 m). The reason
 238 for this mismatch is the lack of camera resolution in the matching of the difference images: For the
 239 camera distance of 494 m, a matching distance of a fraction of a pixel in the orthoimages would result
 240 in the ceilometer cloud height. Due to discretization, this is not possible. Setups using small camera
 241 distances thus undersample pixel-resolution-wise clouds at high altitudes, resulting in scatter.

242 In Fig. 11, the relation between matching distances between the orthoimages of the cameras ($b_1(x, y)$
 243 and $b_2(x, y)$ in Fig. 2, see section 2.1 for explanations) and the ratio of cloud heights and camera distances
 244 is shown. A matching distance of 10 pixels is present if the cloud heights are 10.6 times higher than the
 245 camera distance. The matching distance is 51 pixels if this ratio is 2.1 and drops to 2 if the cloud height
 246 are 53.1 times larger than the camera distance.

247 Figure 11 is derived using equ. 5, which is based on equ. 4 in Kuhn et al. (2018b). In equ. 5, s_{match}
 248 is the matching distance, N is the size of the orthoimage in one dimension, α is the minimum viewing

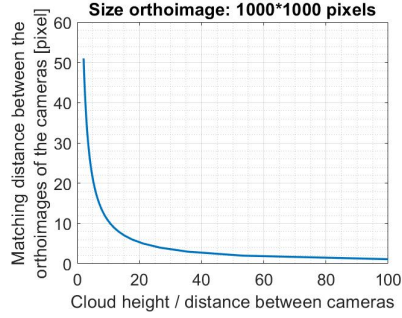


Figure 11: Matching distance between the orthoimages of the cameras in pixel over the ratio of cloud height and camera distance. If the cameras are in close proximity relative to the cloud heights to be measured, the matching distance is small and mismatches / under-sampling occurs.

249 angle, h is the height of the cloud layer and D the distance between the cameras.

$$250 \quad s_{match} = \frac{N}{2 \cdot \tan(90^\circ - \alpha)} \cdot \frac{1}{h/D} \quad (5)$$

251 Figure 12 shows the corresponding cloud height errors divided by the camera distance. A minor
 252 mismatch of one singular pixel has a stronger impact on the expected accuracy if the ratio between cloud
 253 height and camera distance is large.

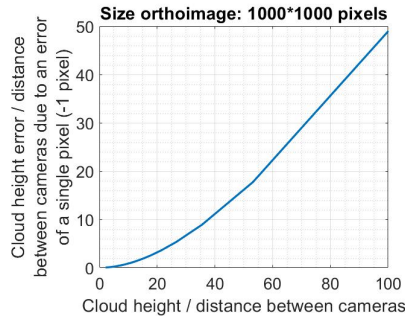


Figure 12: Cloud height errors divided by camera distance caused by a mismatch of one pixel over the ratio of cloud height and camera distance (corresponding to Fig. 11): For small ratios, the such mismatches impact the accuracy stronger than for larger ratios.

254 The undersampling effect shown in Fig. 11 and 12 for large ratios affects the configurations with
 255 camera distance below 1000 m (Fig. 9). This effect is biased for the setup with a camera distance of
 256 771 m towards lower cloud heights. Furthermore, this setup shows little deviations in comparison to
 257 ceilometer measurements for certain periods shown in Fig. 6. The reason for both this bias and the good
 258 agreement on 2017-05-29 remains unclear, but due to the lack of physical information (undersampling)
 259 for high clouds, we opt to not consider this any further.

260 3.2. Explaining deviations for large distances and low clouds

261 In section 2.2, deviations and scatter are found to increase with increased camera distances for low
 262 cloud heights. The reason for this is explained by the concept of overlap. If the cameras are further
 263 apart, the overlap of the cameras' viewing cones is reduced (Fig. 13). Clouds which are not located
 264 inside this overlapping volume are only seen by one camera (or none). The heights of such clouds cannot
 265 be determined. In general, increasing the camera distance reduces the matching area, which makes
 266 mismatches more likely.

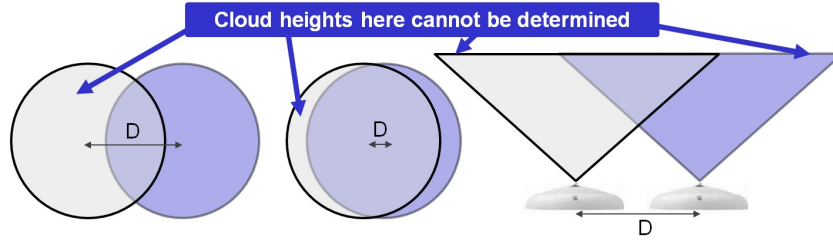


Figure 13: Small distances between the cameras lead to large overlaps. If the cameras are further apart (larger camera distance D), the overlap is reduced.

267 The overlap depends on the ratio of cloud heights and camera distances as shown in Fig. 14. For
 268 instance, for a ratio of 1 (same cloud height and camera distance, e.g. 2 km), the overlap is 86.5 %. If
 269 the cloud height is 4 times greater than the camera distance, the overlap increases to 96.6 %. Similarly,
 270 a ratio of 0.5 results in an overlap of 73.1 %. If the camera distance is 5 times larger than the cloud
 271 height (ratio of 0.2), the overlap is further reduced to 35.7 %. As a comparison, EKO Instruments (2018)
 suggests a ratio of 5 (overlap: 97.3 %) to 7 (overlap: 98.1 %) for optimal accuracy.

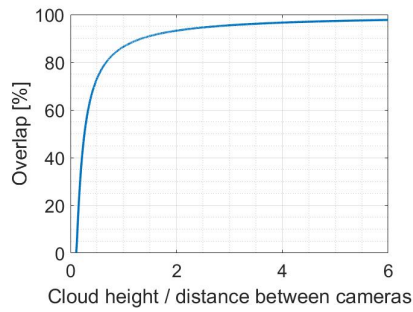


Figure 14: Overlap between two cameras in relation of ratios of cloud heights over camera distances.

272

273 Figure 14 is derived using equ. 6. In equ. 6, R is the radius of the viewing cone with $R = h/\tan(\alpha)$
 274 (h : cloud layer height; α : minimum viewing angle) and D is the distance between the cameras.

275

$$\text{Overlap} = \frac{2 \cdot R^2 \cdot \arccos(D/(2 \cdot R)) - 0.5 \cdot d \cdot \sqrt{4 \cdot R^2 - D^2}}{\pi \cdot R^2} \cdot 100\% \quad (6)$$

276 4. Impacts of the camera hardware and parameters on the optimal camera distance

277 In this section, we link our findings to camera hardware and settings, which enables a limited general-
278 ization and extrapolation to other setups. Section 4.1 considers the impacts of the camera resolution on
279 the optimal distance. The effects of the minimum viewing angle α are studied in section 4.2. Section 4.3
280 briefly discusses the influence of the cloud positions within the all-sky image geometry. The impacts
281 of the image acquisition rate are presented in section 4.4. In section 4.5, further potential impacts on
282 all-sky imager based cloud height estimation deviations are named.

283 4.1. Relation between camera resolution and optimal distance

284 The resolution of the camera is considered to be the most relevant parameter for this study. For
285 example, Janeiro et al. (2012) use a very small camera distance of only 28.9 m in combination with a
286 relatively high resolution camera with 3888×2592 pixels. Here, this relation between camera distances
287 and resolutions is discussed.

288 In this study, the orthoimage has a resolution of 1000×1000 pixels. The orthoimage is derived from
289 the fisheye jpg images and can be set to have a higher resolution. However, due to the lack of information,
290 this artificially higher resolution does not come with higher accuracy. The used all-sky imagers (Mobotix
291 Q24 and older Q25 models) have a resolution of 3 MP. Higher resolution fisheye cameras, e.g. with
292 12 MP or more, are available.

293 With this physically higher resolution, orthoimages with a higher resolution can be employed. For
294 instance, the orthoimage could be $\gamma = \frac{2048}{1536} = 1.\bar{3}$ larger if a 6 MP (2048×3078) camera instead of a
295 3 MP camera (1536×2048) is used. This camera resolution is applied in the new camera model Mobotix
296 Q25, which is used in Nouri et al. (2017). The orthoimage is therefore enlarged by the factor γ in
297 each direction (more detailed calculations are presented in the next sections). This linearly increases
298 the matching distance between the cameras' orthoimages (y -axis in Fig. 11) by a factor of $\gamma' = \gamma \cdot M$,
299 $M = \{x | 1 \leq x \leq \sqrt{2}\}$ (depending on the direction of the matching, diagonal or along the edges of the
300 orthoimage). This factor has a non-linear impact of $1/\tan(\gamma')$ on the accuracy (see Fig. 11 and 12). Thus,
301 higher camera resolutions reduce the required camera distances. This behavior is partially reflected in
302 the distances and resolutions summarized in Tab. 1.

303 4.2. Minimum viewing angle α and optimal camera distance

304 The minimum viewing angle considered so far is $\alpha = 12^\circ$. Several important parameters of the
305 orthoimage depend on this angle, which will be studied here for several camera resolutions. Figure 15
306 shows the elevation angles within a 3 MP jpg fisheye image. In Fig. 16, where the elevation angles of the
307 center row are depicted, we see a linear relation with a gradient of approximately $\pm 0.103^\circ/\text{pixel}$.

308 Although custom lenses exist (e.g. Gutwin and Fedak (2004), Singh et al. (2006), Schmidt et al.
309 (2015)), we assume that the linear relation visible in Fig. 16 holds for most fisheye cameras. Assuming

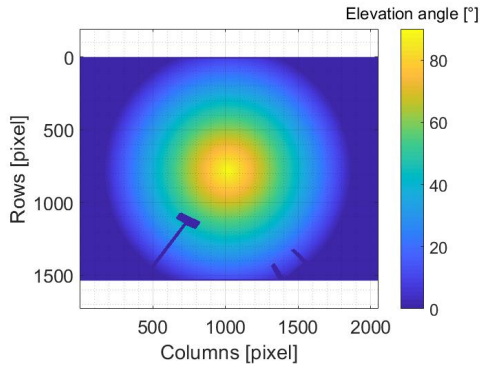


Figure 15: Elevation angles in a 3 MP fisheye raw image.

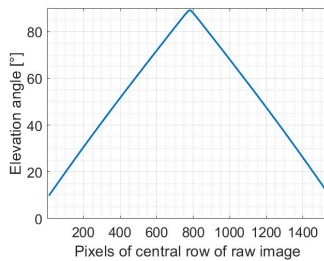


Figure 16: Elevation angles of the center row within a 3 MP fisheye image, corresponding to Fig. 15.

310 furthermore that the first pixel of the center row images a minimum elevation of $\theta_{min} = 0^\circ$ and the
 311 center pixel a maximum elevation of $\theta_{max} = 90^\circ$, the gradient $\Delta\beta$ can be calculated using equ. 7. This
 312 yields a gradient of $0.117^\circ/\text{pixel}$ for a 3 MP image (2048×1536 pixels; due to the symmetry of all-sky
 313 images, the relevant resolution value in this section is always the smaller one.). This calculated gradient
 314 is reasonably close to the gradient shown in Fig. 16.

$$315 \quad \Delta\beta = \frac{\theta_{max} - \theta_{min}}{\Delta\text{pixel indices}} \rightarrow \frac{90^\circ - 0^\circ}{(0.5 \cdot 1536 - 1) \text{ pixels}} = 0.117^\circ/\text{pixels} \quad (7)$$

316 If an orthoimage is generated (see Fig. 17), the center area is compressed into relatively few pixels.
 317 On the other hand, the edge region is stretched. This stretching depends on the minimum viewing angle
 318 α as shown in Fig. 18.

319 Under the assumption of a linear elevation gradient (see equ. 7), the *physical plane-projected resolution*
 320 (*PPR*) can be calculated using equ. 8 with $\Delta\beta$ being the gradient derived in equ. 7, n being the pixel
 321 distance to the center and h being the cloud layer height. The *PPR* describes the physical spatial
 322 resolution within a plane at a given height which depends on the elevation angles of the corresponding
 323 pixels in the raw fisheye image. A visual explanation of the parameters is given in Fig. 19. Figure 20 shows
 324 the relation between elevation angles, camera resolutions and the physical plane-projected resolutions,
 325 normalized by the cloud height.

$$326 \quad PPR = h \cdot (\tan(n \cdot \Delta\beta) - \tan((n - 1) \cdot \Delta\beta)) \quad (8)$$

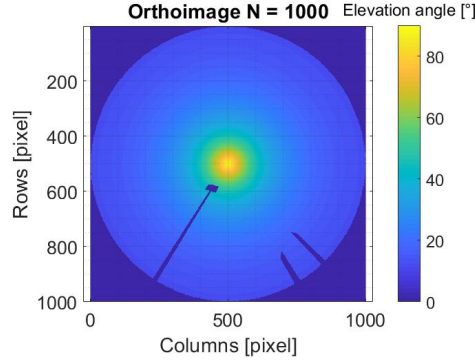


Figure 17: Elevation angles in an orthoimage with a resolution of 1000×1000 pixels and a minimum viewing angle of $\alpha = 12^\circ$, corresponding to Fig. 15. Small minimum viewing angles may lead to extrapolations caused by the lack of physical information.

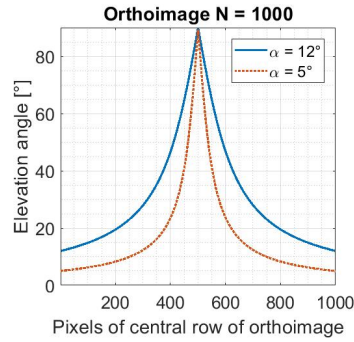


Figure 18: Elevation angles of the center row within an orthoimage with a resolution of 1000×1000 pixels ($N \times N$) and two minimum viewing angles, corresponding to Fig. 15. Smaller minimum viewing angles result in stronger compression of the center area and stretching of the raw fisheye image's edges.

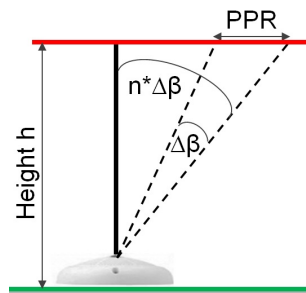


Figure 19: Visual explanations corresponding to equ. 8 and the concept of the physical plane-projected resolution (PPR). $\Delta\beta$ is the gradient derived in equ. 7, which depends on the camera's resolution. The normalized PPR is shown in Fig. 20.

327 We derive from Fig. 20 that a minimum viewing angle of $\alpha = 12^\circ$ corresponds to a PPR normalized
 328 by the cloud height of 0.047 for a camera resolution of 1536 pixels and to a normalized PPR of 0.021 for
 329 a camera resolution of 3456 pixels. For a cloud layer height of 5000 m, this corresponds to a minimum
 330 physical plane-projected resolution of 231.4 m and 104.1 m, respectively. These minimum resolutions

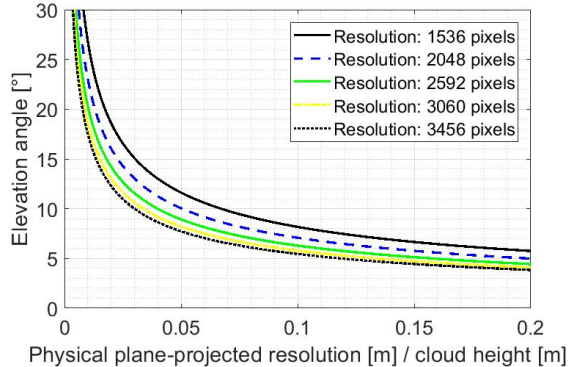


Figure 20: Physical plane-projected resolution (PPR) divided by cloud height shown for elevation angles and camera resolutions, derived from equ. 8.

331 hold for the minimum viewing angle. If we allow such edge pixels to be extrapolated over a maximum
 332 stretching factor of e.g. $\kappa = 5$ pixels in the corresponding orthoimage, the orthoimage has a resolution
 333 of $\frac{235 \text{ m}}{5 \text{ pixels}} = 46.3 \text{ m/pixel}$ or 20.8 m/pixel .

334 The corresponding sizes of the orthoimages are calculated using equ. 9 to be $N = 1009$ pixels and
 335 $N = 2252$ pixels, respectively. In equ. 9, N is the size of the quadratic orthoimage in one dimension,
 336 PPR is the physical plane-projected resolution determined by equ. 8 and κ is the stretching factor for
 337 the least resolved fisheye pixel in the orthoimage.

$$338 \quad N = \frac{2}{\kappa} \cdot \sum_{\zeta_{ele}=\alpha}^{90^\circ} PPR(\zeta_{ele}) \quad (9)$$

339 For a minimum viewing angle of $\alpha = 5^\circ$, the minimum PPR increases to 1293.8 m and 591.9 m . Using
 340 the same resolutions of the orthoimage as before, the orthoimages' sizes expand to $N = 4053$ pixels and
 341 $N = 4015$ pixels, with the least resolved pixel of the fisheye image being stretched over 27.9 pixels or
 342 28.5 pixels in the orthoimage.

343 As a conclusion, a feasible minimum viewing angle must be chosen keeping the physical plane-
 344 projected resolution and the corresponding optimal size of the orthoimage in mind. Large minimum
 345 viewing angles reduce the overlap between the cameras, but are beneficial for the amount of physi-
 346 cal information in the orthoimage. If the minimum viewing angles are small, the chosen resolution of
 347 the orthoimage may become non-physical with singular pixels from the raw image being stretched over
 348 dozens of pixels in the orthoimage, caused by the lack of physical information. This stretching makes
 349 mismatches more likely and thus reduces the expected accuracy, especially for clouds imaged far away
 350 from the center of the all-sky images (see next section).

351 4.3. Impact of cloud positions in relation to the image geometry

352 Using $\Delta\beta$ as defined in equ. 7, the vertical resolution can be calculated, e.g. for a vertical plane
 353 between the cameras as depicted in Fig. 21. This vertical resolution is specified by equ. 10 with D
 354 being the distance between the cameras and n the pixel distance to the center of the raw fisheye image.
 355 Equation 10 is visualized for the $\Delta\beta$ of the used cameras. With a distance between the cameras of
 356 1500 m, the corresponding vertical resolution between the cameras at 10000 m altitude is for instance
 247 m .

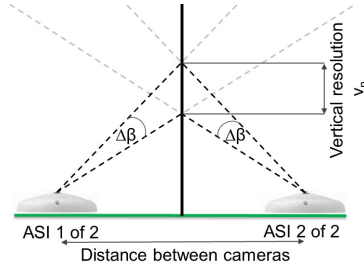


Figure 21: Vertical resolution v_n for a vertical plane between the cameras. The vertical resolution can be calculated using equ. 10, leading to Fig. 22.

357

358
$$v_n = \frac{D}{2} \cdot (\tan(90^\circ - n \cdot \Delta\beta) - \tan(90^\circ - (n - 1) \cdot \Delta\beta)) \quad (10)$$

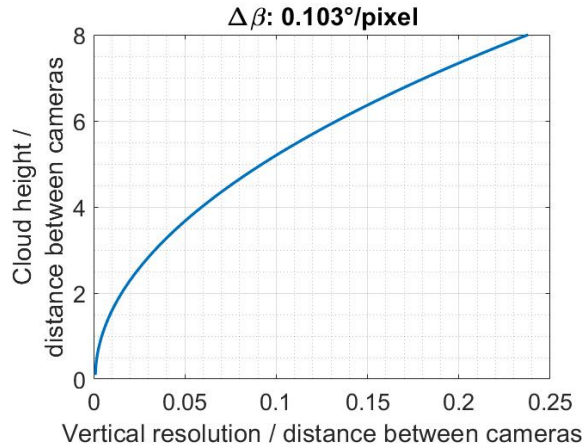


Figure 22: Vertical resolution v_n , calculated using equ. 10 and normalized by the distance between the cameras.

359 This vertical resolution is less resolved for positions far away from the cameras. Thus, the deviations
 360 of cloud height measurements depend on the position of the cloud in relation to the image center. In
 361 general, this relation could be, similar to the discussion in section 4.2, camera-specific. Besides the
 362 reduced vertical resolution, clouds seen under small elevation angles for a camera are imaged in the
 363 distorted edge regions of the fisheye image. There, the calibration accuracy might be worse than in

364 the center. These deviations impact the orthoimage, leading to matching deviations. These deviations
365 depend on the cameras' calibrations and their imaging systems.

366 In addition to that, clouds at the edges of the fisheye all-sky images are rather seen from the side,
367 not from the bottom. This might lead to perspective errors in certain cloud height measurement ap-
368 proaches (Kuhn et al., 2018a). Moreover, as discussed in section 4.2 and shown e.g. in Fig. 17, the
369 physical resolution within the orthoimage decreases towards the edges and pixels from the fisheye raw
370 image might be stretched over several pixels in the orthoimage. This clearly reduces the accuracy of
371 cloud height measurements in these regions.

372 As many of these effects are camera-specific or depend on chosen settings, a general qualitative
373 assessment is not conducted here. However, measured heights of clouds near the center of the images /
374 above the cameras' positions are, based on the considerations presented in this section, estimated to be
375 more accurate.

376 *4.4. Image acquisition rate and optimal camera distance*

377 High temporal resolutions (e.g. 1 s) combined with limited pixel resolutions could lead to an over-
378 sampling effect. This holds for the differential approach used here, which matches differences between
379 subsequent images. If the image acquisition rate is too high, the spatial difference in the cloud positions
380 between two subsequent images could be below the camera resolution. In this scenario, a matching is not
381 possible. Yet, non-subsequent images with larger temporal differences could still be used to obtain cloud
382 heights. On the other hand, very low temporal resolutions larger than 1 min could increase matching
383 errors due to cloud dynamics (blur effects).

384 Other approaches to determine cloud heights from two all-sky imagers are based on two images taken
385 simultaneously by both cameras (e.g. Allmen and Kegelmeyer Jr (1996), Kassianov et al. (2005), Seiz
386 et al. (2007), Nguyen and Kleissl (2014), Beekmans et al. (2016) and Blanc et al. (2017)). In these
387 approaches, the image acquisition rate only determines the amount of measurements per unit of time
388 and does not affect the cloud height determination itself.

389 *4.5. Further factors affecting the accuracy of all-sky imager based cloud height measurements*

390 Besides the parameters impacting the accuracy of all-sky imager based cloud height estimations
391 discussed in the previous sections, further effects are briefly discussed here.

392 Hypothetically, cloud height deviations might correlate to specific cloud types. Arguably, this could
393 be a major challenge for approaches based on matching specific points of interest between images taken
394 by two all-sky imagers. Potentially, this matching might be less robust for cirrus than for cumulus clouds.
395 In general, cumulus clouds are thought to provide easier recognizable features. The differential approach
396 used here, which matches differences, might show less dependency of cloud types. However, this has not
397 been studied.

398 Another factor impacting all-sky imager derived cloud heights is the accuracy of the interior and
399 exterior orientations. For the interior orientation, well established toolboxes as the one used here (Scara-
400 muzza et al., 2006) are available. However, small deviations cannot be avoided completely. The exterior
401 orientation can be obtained by tracking e.g. star constellations or the moon, with the latter being done
402 for the cameras in this study. Besides certain uncertainties present in these approaches, the exterior
403 orientation might also be affected by e.g. thermal expansion of support structures beneath the cam-
404 eras, causing shifts in the camera’s position. Due to geometrical properties, these factors are thought
405 to have their strongest impact on clouds near the horizon of the all-sky images. Besides initial accurate
406 determinations of the orientations, continuous monitoring could limit the corresponding deviations. Fur-
407 thermore, as realized in Nouri et al. (2018b), several redundant pairs of cameras could be used to detect
408 and correct erroneous measurements of one specific configuration.

409 One main challenge for all-sky imagers is soiling as their upward facing lens is exposed to the elements.
410 Using the differential approach, stationary dirt does not cause mismatching, but might lead to the
411 occlusion of clouds. Soiling is considered the major challenge for all approaches based on matching
412 stationary points of interests or segmented cloud masks.

413 5. Further aspects relevant for the optimal camera distance

414 As shown in the previous sections, the distance between the cameras of an all-sky imager system
415 impacts its ability to accurately determine cloud heights. However, besides cloud heights, the camera
416 distance is of importance for other parameters as well.

417 If, for instance, a network of relatively independent all-sky imagers shall cover an area as large
418 as possible, the overlap should be reduced to the required minimum. The derivation of cloud height
419 information is thus more difficult or even impossible. However, depending on the application, cloud
420 height information might be less relevant or could be externally provided to the cameras. Such exam-
421 ple applications are the all-sky imager based detection of solar variability classes (e.g. Stefferud et al.
422 (2012), Nouri et al. (2018)), cloud coverage (e.g. Ackerman and Cox (1981), Tapakis and Charalam-
423 bides (2013), Jayadevan et al. (2015), Dev et al. (2017), Kuhn et al. (2017)), cloud type classifications
424 (e.g. Heinle et al. (2010), Martínez-Chico et al. (2011), Kazantzidis et al. (2012), Taravat et al. (2015), Xia
425 et al. (2015)) or camera-derived solar irradiance measurements (e.g. Tohsing et al. (2013), Tohsing et al.
426 (2014), Tzoumanikas et al. (2016)).

427 Furthermore, for certain applications, low clouds are more important than high clouds, e.g. for not
428 instrument-rated pilots (e.g. Hunter (2002), Atsushi (2004), Fultz and Ashley (2016)). Therefore, the
429 focus of the application has an impact on the optimal camera distance. In practice, however, maximum
430 distances between the cameras of nowcasting systems are often defined by property boundaries or the
431 availability of infrastructure.

432 *Optimal orientation of the cameras.* A question related to the optimal camera question is the optimal
433 orientation of the cameras, which is briefly addressed in Massip et al. (2015). Depending on the pre-
434 dominant cloud motion direction, the intended application and algorithmic approaches, an orientation
435 of the two cameras' axis in parallel or orthogonal to the main cloud motion direction is preferable. An
436 orientation orthogonal to the main cloud motion direction is, to a minor degree, superior for cloud height
437 measurements as clouds coming from this main direction are seen by both cameras at a similar time,
438 enabling earlier cloud height derivations for clouds with motion vectors aligned with the axis of the two
439 cameras. If the early detection of clouds is more important than their heights, an orientation in parallel
440 with the main cloud motion direction is more appropriate. Moreover, if a cloud field is approaching the
441 cameras, one cloud motion vector and one cloud height could be derived from the foremost cloud and
442 extrapolated to the whole cloud field.

443 **6. Quantitative generalization of the findings to other all-sky imager based cloud height** 444 **measurement approaches**

445 In this section, we try to generalize our findings to other all-sky imager based cloud height mea-
446 surement approaches. We discuss several competing algorithms. Methods only validated in simulations
447 (e.g. Kassianov et al. (2005), Mejia et al. (2018)) are not considered.

448 At first, the method presented in Blanc et al. (2017) is summarized. This approach is based on a
449 binary cloud segmentation, which classifies each pixel into clouded or cloud-free. Certain clouded pixels
450 are selected within the considered image of one all-sky imager based on texture and contrast information
451 to be tie points for the cloud height estimation. The matching is conducted using one image of a second
452 all-sky imager by maximizing the correlation between the images starting at an assumed cloud height
453 of 4500 m. A k-Nearest-Neighbor classifier is used to distinguish up to five different cloud layers. Areas
454 between the tie points are extrapolated. This way, a cloud height is assigned to every clouded pixel. This
455 algorithm was validated on one day using camera hardware also used in this study. For this setup, the
456 discussions on the relation between camera distance and camera resolution, e.g. regarding the vertical
457 resolution, hold without adaption. Also, the considerations of the impacts of cloud positions within the
458 all-sky images (see section 4.3) and the image acquisition rate (see section 4.4), which only defines the
459 amount of measurements per time in this approach, are directly applicable. As no orthoimage is used
460 in this algorithm, certain ideas mentioned in section 4.1 must be modified. Potentially, the effects of
461 different cloud types on the deviations, which are discussed in section 4.5, are more relevant for this
462 approach than for the differential approach used here.

463 In Nguyen and Kleissl (2014), a method based on two all-sky imagers is validated on four days. Using
464 16-bit depth saturation images, matching is conducted within orthoimages ("*georeference projection of*
465 *sky images*" Nguyen and Kleissl (2014)). These orthoimages have minimum elevation angles of $\alpha = 20^\circ$.

466 This approach provides one cloud height for each set of all-sky images. Due to the similarity of the
467 algorithms, we think that all findings not directly related to the differential approach can be applied
468 to this method. However, matching saturation images might be more prone to perspective challenges,
469 especially for camera distances larger than the distance of 1230 m used in Nguyen and Kleissl (2014).
470 Another approach based on matching points of interest is also introduced, which is found to be less
471 robust in comparison to the single layer approach, especially for multi-layer cloud situations.

472 The differential approach used here was further developed and benchmarked on 30 days in Nouri et al.
473 (2018b). This further development includes the capability to derive multiple cloud heights from a pair of
474 all-sky images. A configuration based on two all-sky imagers and a configuration based on four all-sky
475 imagers, both using this modified differential approach, are compared to a voxel-carving and segmentation
476 based system using the same camera hardware (Nouri et al., 2018b). The latter system was significantly
477 outperformed by the configurations using the differential approach. Due to inherent redundancies, the
478 four camera differential configuration achieved an MAD of 17 %. For the two camera setup with the
479 modified differential approach, an MAD of 29 % was found. The voxel-carving based system yielded an
480 MAD of 46 %. All findings presented here are directly applicable to the two differential systems. This
481 does not hold for the third configuration: For voxel-carving approaches, the camera distances should
482 ideally be larger than the expected cloud dimensions.

483 **7. Step-by-step guide to determine the optimal distance between cameras and further** 484 **required parameters for all-sky imager based cloud height measurements**

485 We start with the assumption of having two cameras with the same resolution. The cameras are
486 further assumed to have standard fisheye lenses, which hypothetically show a linear relation between the
487 imaged elevations and the pixels similar to Fig. 16. In the following, the relevant configuration parameters
488 are derived step by step. This list is, to a certain degree, specific for the algorithmic approach used in
489 this study.

- 490 1. Calculate the gradient $\Delta\beta$, adapting equ. 7 to the used camera hardware.
- 491 2. Calculate the PPR using equ. 8.
- 492 3. Chose the minimum viewing angle α as large as possible for your application. For most applications,
493 angles of $\alpha = \{\alpha | 10^\circ \leq \alpha \leq 30^\circ\}$ are considered to be feasible.
- 494 4. Define the minimum PPR /cloud height based on the minimum viewing angle α and equ. 8, shown
495 in Fig. 20.
- 496 5. Chose the maximum stretching factor κ between the fisheye jpg image pixel at the minimum viewing
497 angle and the corresponding pixel in the orthoimage. A reasonable stretching factor for these edge
498 pixels is thought to be 5.

- 499 6. Define the cloud height h , which is considered most important for your application. Relevant
500 heights could be between $h = \{h | 100 \text{ m} \leq h \leq 10 \text{ km}\}$.
- 501 7. Calculate the minimum resolution res_{min} in the orthoimage with $res_{min} = PPR_{min}/k$. Is this
502 minimum resolution feasible for your application? If this is not the case, you might reconsider
503 the minimum viewing angle α or the required camera resolution. A res_{min} (far) smaller than
504 100 m/pixel is thought to be adequate.
- 505 8. Calculate the optimal size $N \times N$ of the orthoimage using equ. 9.
- 506 9. Define the minimum matching distance s_{match} . Reasonable minimum matching distances are con-
507 sidered to be around 10 pixels. From this minimum matching distance and the relevant cloud
508 height h , the distance between the cameras D can be derived using equ. 5.
- 509 10. Control the overlap of the cameras' viewing cones with equ. 6. Arguably, this overlap should be
510 larger than 95 % for most applications. You may also like to check the vertical resolutions at
511 relevant distances from your setup using equ. 10.

512 If camera distances are defined by local infrastructure, calculate backwards to assure the feasibility
513 or assess limitations of the imposed distance.

514 8. Conclusion

515 We aimed at identifying the optimal camera distance of a cloud height measurement system consisting
516 of two all-sky imagers. An in-field study on 93 days, using 7 configurations, is presented and the
517 findings are explained using modeling. For the used configuration and all cloud heights, an optimal
518 camera distance of approximately 1500 m appears to be best suited. Smaller camera distances result in
519 undersampling effects for clouds at high altitudes. Larger camera distances do not improve the deviations
520 found for high clouds but introduce (to a minor extent) scatter, especially for low clouds. This is caused
521 by a reduced overlap in the cameras' fields of view.

522 We consider the resolution of the camera the most important lever to utilize if small camera distances
523 are needed. We estimate that camera distances between 500 m and 1000 m are feasible for camera resolu-
524 tions at and above 6 MP, which mostly corresponds to parameters used in the literature: For instance, Hu
525 et al. (2009) use the same camera resolution (2048×1536 pixels) and a camera distance of 1500 m. Similar
526 distances and resolutions are used by Nguyen and Kleissl (2014) (1230 m, 1750×1750 pixels) and Öktem
527 et al. (2014) (1000 m, 1296×960 pixels / 1024×768 pixels). Smaller camera distances and higher camera
528 resolutions are used by Seiz et al. (2007) (850 m, 3060×2036 pixels / 3072×2048 pixels), Roy (2016)
529 (590 m, 2560×1920 pixels), Beekmans et al. (2016) (300 m, 2448×2048 pixels) and Savoy et al. (2017)
530 (100 m, 5184×3456 pixels). These combinations of camera resolution and distance are in alignment with
531 our findings.

532 In Andreev et al. (2014), a camera distance of 17 m and a resolution of 3072×2304 pixels are used.
533 Our findings indicate that this combination is only feasible for low clouds, which is confirmed in Andreev
534 et al. (2014): The deviation estimation reaches 50 % for cloud heights of 2000 m and the authors
535 state that the accuracy can be improved by "*increasing the distance between the cameras or use higher*
536 *image resolutions*" (Andreev et al. (2014)). Janeiro et al. (2012) (28.9 m, 3888×2592 pixels) validate the
537 obtained cloud heights on one day with two cloud layers (1500 m and 6000 m), showing good agreement
538 to a reference ceilometer. They note that the vertical resolution for clouds at 6000 m is only 350 m
539 and that this "*problem can be reduced by increasing the distance between the two cameras*" (Janeiro
540 et al. (2012)). The combinations of camera resolution and distances used in Katai-Urban et al. (2016)
541 (90 m, 5184×3456 pixels) and Katai-Urban et al. (2018) (90/100/130 m, 5184×3456 pixels) as well as
542 the modeling conducted there also agree with our findings as the focus in these publications is on low
543 clouds.

544 Some publications use combinations of camera resolution and distances which are not in accordance
545 with our findings. For instance, Kassianov et al. (2005) *models* that 352×288 pixels cameras with a
546 distance of 540 m could be feasible. We think that such a setup would only be feasible for low clouds and
547 faces difficulties while determining the altitudes of high clouds. On the other hand, we are convinced
548 that the setup used by Allmen and Kegelmeyer Jr (1996) (5540 m, 256×256 pixels) cannot determine
549 low cloud heights due to the lack of overlap.

550 Voxel-carving approaches (e.g. Nouri et al. (2017), Kuhn et al. (2017), Mejia et al. (2018)) model
551 a 3-dimensional cloud form out of the different viewing geometries of the cameras. For this approach,
552 the viewing geometries must be as different as possible, which lets larger camera distances appear more
553 reasonable. Hence, besides the discussions on the overlap between the cameras, the findings in this study
554 are not directly applicable to voxel carving systems. With the exception of voxel-carving, we estimate
555 that the findings here hypothetically hold for a large variety of algorithmic approaches presented in the
556 literature.

557 Future work could include a comprehensive comparison of different algorithmic approaches for all-sky
558 imager based cloud height estimations. Moreover, potential dependencies of cloud height deviations and
559 cloud types should be studied, using cloud classification algorithms for all-sky images such as presented
560 e.g. in Heinle et al. (2010), Kazantzidis et al. (2012) or Huertas-Tato et al. (2017). In Nouri et al.
561 (2018b), the differential approach used here was expanded to derive several cloud heights within the
562 all-sky images. Using only one ceilometer, the accuracy of such measurements is difficult to evaluate.
563 Moreover, a likely relation between cloud height deviations and the distance as well as the orientation
564 of the clouds to the all-sky imagers cannot be studied. However, drastic cost reductions in LIDAR
565 technology, which are caused by the development of autonomous cars, could enable affordable spatially
566 resolved cloud height measurements. In the near future, this could be achieved by employing many low

567 cost LIDAR systems, which are spatially distributed over several square kilometers.

568 As a conclusion, all-sky imager based systems can automatically measure multiple cloud heights at
569 once, derive cloud types and cloud coverage as well as cloud motion vectors. Therefore, such low cost
570 and robust devices might be the key meteorological instrument in the near future.

571 Acknowledgements

572 The European Union's FP7 program under Grant Agreement no. 608623 (DNICast project) financed
573 operations of the all-sky imagers. With funding from the German Federal Ministry for Economic Affairs
574 and Energy within the WobaS project, all-sky imager systems were further developed.

575 References

576 References

577 Ackerman, S.A., Cox, S.K., 1981. Comparison of Satellite and All-Sky Camera Estimates of Cloud
578 Cover during GATE. *Journal of Applied Meteorology* 20, 581–587. URL: [https://doi.org/
579 10.1175/1520-0450\(1981\)020<0581:COASAAS>2.0.CO;2](https://doi.org/10.1175/1520-0450(1981)020<0581:COASAAS>2.0.CO;2), doi:10.1175/1520-0450(1981)020<0581:
580 COASAAS>2.0.CO;2.

581 Allmen, M.C., Kegelmeyer Jr, W.P., 1996. The Computation of Cloud-Base Height from Paired Whole-
582 Sky Imaging Cameras. *Journal of Atmospheric and Oceanic Technology* 13, 97–113. URL: [https:
583 //doi.org/10.1175/1520-0426\(1996\)013<0097:TCOCBH>2.0.CO;2](https://doi.org/10.1175/1520-0426(1996)013<0097:TCOCBH>2.0.CO;2).

584 Andreev, M.S., Chulichkov, A.I., Emilenko, A.S., Medvedev, A.P., Postylyakov, O.V., 2014. Estimation
585 of cloud height using ground-based stereophotography: methods, error analysis and validation. *Proc.*
586 *SPIE* 9259, 92590N–92590N–6. URL: [http://proceedings.spiedigitallibrary.org/proceeding.
587 asp?articleid=1974843](http://proceedings.spiedigitallibrary.org/proceeding.aspx?articleid=1974843), doi:10.1117/12.2069800.

588 Atsushi, T., 2004. Fatal miscommunication: English in aviation safety. *World*
589 *Englishes* 23, 451–470. URL: [https://onlinelibrary.wiley.com/doi/abs/
590 10.1111/j.0883-2919.2004.00368.x](https://onlinelibrary.wiley.com/doi/abs/10.1111/j.0883-2919.2004.00368.x), doi:10.1111/j.0883-2919.2004.00368.x,
591 arXiv:<https://onlinelibrary.wiley.com/doi/pdf/10.1111/j.0883-2919.2004.00368.x>.

592 Beekmans, C., Schneider, J., Läbe, T., Lennefer, M., Stachniss, C., Simmer, C., 2016. Cloud photogram-
593 metry with dense stereo for fisheye cameras. *Atmospheric Chemistry and Physics* 16, 14231–14248.
594 URL: <http://dx.doi.org/10.5194/acp-16-14231-2016>, doi:10.5194/acp-16-14231-2016.

595 Bernecker, D., Riess, C., Christlein, V., Angelopoulou, E., Hornegger, J., 2013. Representation Learning
596 for Cloud Classification. Springer Berlin Heidelberg, Berlin, Heidelberg. URL: [http://dx.doi.org/
597 10.1007/978-3-642-40602-7_42](http://dx.doi.org/10.1007/978-3-642-40602-7_42).

598 Blanc, P., Massip, P., Kazantzidis, A., Tzoumanikas, P., Kuhn, P., Wilbert, S., Schüler, D., Prah, C.,
599 2017. Short-Term Forecasting of High Resolution Local DNI Maps with Multiple Fish-Eye Cameras in
600 Stereoscopic Mode. AIP Conference Proceedings 1850, 140004. URL: [http://aip.scitation.org/](http://aip.scitation.org/doi/abs/10.1063/1.4984512)
601 [doi/abs/10.1063/1.4984512](http://aip.scitation.org/doi/abs/10.1063/1.4984512), doi:10.1063/1.4984512.

602 Campbell, J.R., Peterson, D.A., Marquis, J.W., Fochesatto, G.J., Vaughan, M.A., Stewart, S.A., Tackett,
603 J.L., Lolli, S., Lewis, J.R., Oyola, M.I., Welton, E.J., 2018. Unusually Deep Wintertime Cirrus Clouds
604 Observed over the Alaskan Subarctic. Bulletin of the American Meteorological Society 99, 27–32.
605 URL: <https://doi.org/10.1175/BAMS-D-17-0084.1>, doi:10.1175/BAMS-D-17-0084.1.

606 Chu, Y., Pedro, H.T., Kaur, A., Kleissl, J., Coimbra, C.F., 2017. Net load forecasts for solar-
607 integrated operational grid feeders. Solar Energy 158, 236 – 246. URL: [http://www.sciencedirect.](http://www.sciencedirect.com/science/article/pii/S0038092X17308393)
608 [com/science/article/pii/S0038092X17308393](http://www.sciencedirect.com/science/article/pii/S0038092X17308393), doi:[https://doi.org/10.1016/j.solener.2017.](https://doi.org/10.1016/j.solener.2017.09.052)
609 [09.052](https://doi.org/10.1016/j.solener.2017.09.052).

610 Damiani, R., Zehnder, J., Geerts, B., Demko, J., Haimov, S., Petti, J., Poulos, G.S., Razdan, A., Hu, J.,
611 Leuthold, M., French, J., 2008. The Cumulus, Photogrammetric, In Situ, and Doppler Observations
612 Experiment of 2006. Bulletin of the American Meteorological Society 89, 57–74. URL: [https://doi.](https://doi.org/10.1175/BAMS-89-1-57)
613 [org/10.1175/BAMS-89-1-57](https://doi.org/10.1175/BAMS-89-1-57), doi:10.1175/BAMS-89-1-57.

614 Dev, S., Lee, Y.H., Winkler, S., 2017. Color-Based Segmentation of Sky/Cloud Images From Ground-
615 Based Cameras. IEEE Journal of Selected Topics in Applied Earth Observations and Remote Sensing
616 10, 231–242. URL: <http://ieeexplore.ieee.org/document/7471439/>, doi:10.1109/JSTARS.2016.
617 [2558474](http://ieeexplore.ieee.org/document/7471439/).

618 EKO Instruments, 2018. All Sky Imager Cloud Base Height Software ASI-16. Technical Re-
619 port. EKO Instruments B.V. URL: [https://media.eko-eu.com/assets/media/EKO_ASI16Manual_](https://media.eko-eu.com/assets/media/EKO_ASI16Manual_CloudBaseHeight_.pdf)
620 [CloudBaseHeight_.pdf](https://media.eko-eu.com/assets/media/EKO_ASI16Manual_CloudBaseHeight_.pdf).

621 Fultz, A.J., Ashley, W.S., 2016. Fatal weather-related general aviation accidents in the united
622 states. Physical Geography 37, 291–312. URL: <https://doi.org/10.1080/02723646.2016.1211854>,
623 [doi:10.1080/02723646.2016.1211854](https://doi.org/10.1080/02723646.2016.1211854).

624 Gaumet, J.L., Heinrich, J.C., Cluzeau, M., Pierrard, P., Prieur, J., 1998. Cloud-Base Height Measure-
625 ments with a Single-Pulse Erbium-Glass Laser Ceilometer. Journal of Atmospheric and Oceanic Tech-
626 nology 15, 37–45. URL: [https://doi.org/10.1175/1520-0426\(1998\)015<0037:CBHMWA>2.0.CO;2](https://doi.org/10.1175/1520-0426(1998)015<0037:CBHMWA>2.0.CO;2),
627 [doi:10.1175/1520-0426\(1998\)015<0037:CBHMWA>2.0.CO;2](https://doi.org/10.1175/1520-0426(1998)015<0037:CBHMWA>2.0.CO;2).

628 Gutwin, C., Fedak, C., 2004. A comparison of fisheye lenses for interactive layout tasks, in: Proceedings
629 of Graphics Interface 2004, Canadian Human-Computer Communications Society, School of Computer

630 Science, University of Waterloo, Waterloo, Ontario, Canada. pp. 213–220. URL: [http://dl.acm.org/](http://dl.acm.org/citation.cfm?id=1006058.1006084)
631 [citation.cfm?id=1006058.1006084](http://dl.acm.org/citation.cfm?id=1006058.1006084).

632 Heinle, A., Macke, A., Srivastav, A., 2010. Automatic cloud classification of whole sky images. *At-*
633 *mospheric Measurement Techniques* 3, 557. URL: <http://dx.doi.org/10.5194/amt-3-557-2010>,
634 [doi:10.5194/amt-3-557-2010](https://doi.org/10.5194/amt-3-557-2010).

635 Hu, J., Razdan, A., Zehnder, J.A., 2009. Geometric Calibration of Digital Cameras for 3D Cumulus
636 Cloud Measurements. *Journal of Atmospheric and Oceanic Technology* 26, 200–214. URL: <https://doi.org/10.1175/2008JTECHA1079.1>, [doi:10.1175/2008JTECHA1079.1](https://doi.org/10.1175/2008JTECHA1079.1).

638 Huertas-Tato, J., Rodríguez-Benítez, F.J., Arbizu-Barrena, C., Aler-Mur, R., Galvan-Leon, I., Pozo-
639 Vázquez, D., 2017. Automatic Cloud-Type Classification Based On the Combined Use of a Sky
640 Camera and a Ceilometer. *Journal of Geophysical Research: Atmospheres* 122, 11,045–11,061. URL:
641 <https://doi.org/10.1002/2017JD027131>.

642 Hunter, D.R., 2002. Risk perception and risk tolerance in aircraft pilots. Technical Report. Federal
643 Aviation Administration Washington DC Office of Aviation Medicine. URL: [http://www.dtic.mil/](http://www.dtic.mil/dtic/tr/fulltext/u2/a407997.pdf)
644 [dtic/tr/fulltext/u2/a407997.pdf](http://www.dtic.mil/dtic/tr/fulltext/u2/a407997.pdf).

645 Janeiro, F.M., Carretas, F., Kandler, K., Ramos, P.M., Wagner, F., 2012. Automated cloud base
646 height and wind speed measurement using consumer digital cameras. XX IMEKO World Congr URL:
647 <http://dspace.uevora.pt/rdpc/handle/10174/5420>.

648 Jayadevan, V.T., Rodriguez, J.J., Cronin, A.D., 2015. A new contrast-enhancing feature for cloud
649 detection in ground-based sky images. *Journal of Atmospheric and Oceanic Technology* 32, 209–
650 219. URL: <https://doi.org/10.1175/JTECH-D-14-00053.1>, [doi:10.1175/JTECH-D-14-00053.1](https://doi.org/10.1175/JTECH-D-14-00053.1),
651 [arXiv:https://doi.org/10.1175/JTECH-D-14-00053.1](https://doi.org/10.1175/JTECH-D-14-00053.1).

652 Johnson, R.W., Hering, W.S., Shields, J.E., 1989. Automated Visibility & Cloud Cover Measurements
653 with a Solid State Imaging System. Technical Report. SCRIPPS INSTITUTION OF OCEANOGRAP-
654 PHY LA JOLLA CA MARINE PHYSICAL LAB. URL: [http://www.dtic.mil/docs/citations/](http://www.dtic.mil/docs/citations/ADA216906)
655 [ADA216906](http://www.dtic.mil/docs/citations/ADA216906).

656 Kassander, A.R., Sims, L.L., 1957. CLOUD PHOTOGRAMMETRY WITH GROUND-LOCATED
657 K-17 AERIAL CAMERAS. *Journal of Meteorology* 14, 43–49. URL: [https://doi.org/10.1175/](https://doi.org/10.1175/0095-9634-14.1.43)
658 [0095-9634-14.1.43](https://doi.org/10.1175/0095-9634-14.1.43), [doi:10.1175/0095-9634-14.1.43](https://doi.org/10.1175/0095-9634-14.1.43).

659 Kassianov, E., Long, C.N., Christy, J., 2005. Cloud-Base-Height Estimation from Paired Ground-Based
660 Hemispherical Observations. *Journal of Applied Meteorology* 44, 1221–1233. URL: [http://dx.doi.](http://dx.doi.org/10.1175/JAM2277.1)
661 [org/10.1175/JAM2277.1](http://dx.doi.org/10.1175/JAM2277.1), [doi:10.1175/JAM2277.1](https://doi.org/10.1175/JAM2277.1).

- 662 Katai-Urban, G., Eichhardt, I., Otte, V., Megyesi, Z., Bixel, P., 2018. Reconstructing atmo-
663 spheric cloud particles from multiple fisheye cameras. *Solar Energy* 171, 171 – 184. URL: <http://www.sciencedirect.com/science/article/pii/S0038092X18306017>, doi:<https://doi.org/10.1016/j.solener.2018.06.050>.
- 666 Katai-Urban, G., Otte, V., Kees, N., Megyesi, Z., Bixel, P., 2016. STEREO RECONSTRUC-
667 TION OF ATMOSPHERIC CLOUD SURFACES FROM FISHEYE CAMERA IMAGES. *International Archives of the Photogrammetry, Remote Sensing & Spatial Information Sciences*
668 41. URL: [https://www.int-arch-photogramm-remote-sens-spatial-inf-sci.net/XLI-B3/49/](https://www.int-arch-photogramm-remote-sens-spatial-inf-sci.net/XLI-B3/49/2016/isprs-archives-XLI-B3-49-2016.pdf)
670 [2016/isprs-archives-XLI-B3-49-2016.pdf](https://www.int-arch-photogramm-remote-sens-spatial-inf-sci.net/XLI-B3/49/2016/isprs-archives-XLI-B3-49-2016.pdf).
- 671 Kazantzidis, A., Tzoumanikas, P., Bais, A., Fotopoulos, S., Economou, G., 2012. Cloud detection and
672 classification with the use of whole-sky ground-based images. *Atmospheric Research* 113, 80–88. URL:
673 <http://dx.doi.org/10.1016/j.atmosres.2012.05.005>, doi:10.1016/j.atmosres.2012.05.005.
- 674 Kuhn, P., Bijan Nouri, S.W., Bianco, L., Vallance, L., Prah, C., Ramirez, L., Zarzalejo, L., Schmidt, T.,
675 Yasser, Z., Vuilleumier, L., Heinemann, D., Kazantzidis, A., Wilczak, J.M., Blanc, P., Pitz-Paal, R.,
676 2018a. Vergleich und Bewertung solarer Nowcasting-Systeme, in: conexio GmbH (Ed.), *Tagungsunter-*
677 *lagen PV-Symposium 2018*. URL: [http://www.pv-symposium.de/programm/tagungsunter-](http://www.pv-symposium.de/programm/tagungsunterlagen.html)
678 [lagen.html](http://www.pv-symposium.de/programm/tagungsunterlagen.html).
- 679 Kuhn, P., Nouri, B., Wilbert, S., Prah, C., Kozonek, N., Schmidt, T., Yasser, Z., Ramirez, L., Zarzalejo,
680 L., Meyer, A., Vuilleumier, L., Heinemann, D., Blanc, P., Pitz-Paal, R., 2017. Validation of an all-sky
681 imager-based nowcasting system for industrial PV plants. *Progress in Photovoltaics: Research and*
682 *Applications* 26, 608–621. URL: <http://dx.doi.org/10.1002/pip.2968>, doi:10.1002/pip.2968.
683 pIP-17-122.R1, cover article: 10.1002/pip.3065.
- 684 Kuhn, P., Wirtz, M., Killius, N., Wilbert, S., Bosch, J., Hanrieder, N., Nouri, B., Kleissl, J., Ramirez,
685 L., Schroedter-Homscheidt, M., Heinemann, D., Kazantzidis, A., Blanc, P., Pitz-Paal, R., 2018b.
686 Benchmarking three low-cost, low-maintenance cloud height measurement systems and ecmwf cloud
687 heights against a ceilometer. *Solar Energy* 168, 140 – 152. URL: <http://www.sciencedirect.com/science/article/pii/S0038092X1830183X>, doi:[https://doi.org/10.1016/j.solener.2018.](https://doi.org/10.1016/j.solener.2018.02.050)
688 [02.050](https://doi.org/10.1016/j.solener.2018.02.050). *advances in Solar Resource Assessment and Forecasting*.
- 690 Martínez-Chico, M., Batlles, F., Bosch, J., 2011. Cloud classification in a mediterranean location using
691 radiation data and sky images. *Energy* 36, 4055–4062. URL: [http://dx.doi.org/10.1016/j.energy.](http://dx.doi.org/10.1016/j.energy.2011.04.043)
692 [2011.04.043](http://dx.doi.org/10.1016/j.energy.2011.04.043), doi:10.1016/j.energy.2011.04.043.
- 693 Martucci, G., Milroy, C., O’Dowd, C.D., 2010. Detection of Cloud-Base Height Using Jenoptik CHM15K

694 and Vaisala CL31 Ceilometers. *Journal of Atmospheric and Oceanic Technology* 27, 305–318. URL:
695 <http://dx.doi.org/10.1175/2009JTECHA1326.1>, doi:10.1175/2009JTECHA1326.1.

696 Massip, P., Blanc, P., Kazantzidis, A., Tzoumanikas, P., 2015. Report on algorithms for nowcasting
697 methods based on sky imagers. DNICast deliverable 3.1 URL: <http://www.dnicast-project.net>.

698 Mecikalski, J.R., Feltz, W.F., Murray, J.J., Johnson, D.B., Bedka, K.M., Bedka, S.T., Wimmers, A.J.,
699 Pavolonis, M., Berendes, T.A., Haggerty, J., Minnis, P., Bernstein, B., Williams, E., 2007. Aviation
700 Applications for Satellite-Based Observations of Cloud Properties, Convection Initiation, In-Flight
701 Icing, Turbulence, and Volcanic Ash. *Bulletin of the American Meteorological Society* 88, 1589–1607.
702 URL: <https://doi.org/10.1175/BAMS-88-10-1589>, doi:10.1175/BAMS-88-10-1589.

703 Mejia, F.A., Kurtz, B., Levis, A., Íñigo de la Parra, Kleissl, J., 2018. Cloud tomography applied to
704 sky images: A virtual testbed. *Solar Energy* 176, 287 – 300. URL: [https://doi.org/10.1016/j.](https://doi.org/10.1016/j.solener.2018.10.023)
705 [solener.2018.10.023](https://doi.org/10.1016/j.solener.2018.10.023).

706 Müller, R., Haussler, S., Jerg, M., 2018. The Role of NWP Filter for the Satellite Based Detection
707 of Cumulonimbus Clouds. *Remote Sensing* 10. URL: <http://www.mdpi.com/2072-4292/10/3/386>,
708 doi:10.3390/rs10030386.

709 Nguyen, D.A., Kleissl, J., 2014. Stereographic methods for cloud base height determination using two sky
710 imagers. *Solar Energy* 107, 495–509. URL: <http://dx.doi.org/10.1016/j.solener.2014.05.005>,
711 doi:10.1016/j.solener.2014.05.005.

712 Nouri, B., Kuhn, P., Wilbert, S., Hanrieder, N., Prah, C., Zarzalejo, L., Kazantzidis, A., Blanc, P., Pitz-
713 Paal, R., 2018b. Cloud height and tracking accuracy of three all sky imager systems for individual
714 clouds. *Solar Energy*, accepted with minor revisions .

715 Nouri, B., Kuhn, P., Wilbert, S., Prah, C., Pitz-Paal, R., Blanc, P., Schmidt, T., Yasser, Z., Santigosa,
716 L.R., Heinemann, D., 2017. Nowcasting of DNI Maps for the Solar Field Based on Voxel Carving
717 and Individual 3D Cloud Objects from All Sky Images. *SolarPACES 2017*, to be published in AIP
718 Conference Proceedings .

719 Nouri, B., Wilbert, S., Hanrieder, N., Kuhn, P., Schroedter-Homscheidt, M., Pitz-Paal, R., Zarzalejo,
720 L., Kumar, S., Goswami, N., Shankar, R., Affolter, R., 2018. Intra-hour classification of direct normal
721 irradiance for two sites in Spain and India. *SolarPACES 2018*, to be published in AIP Conference
722 Proceedings .

723 Öktem, R., Prabhat, Lee, J., Thomas, A., Zuidema, P., Romps, D.M., 2014. Stereophotogrammetry
724 of Oceanic Clouds. *Journal of Atmospheric and Oceanic Technology* 31, 1482–1501. URL: <https://doi.org/10.1175/JTECH-D-13-00224.1>, doi:10.1175/JTECH-D-13-00224.1.

726 Orville, H.D., Jr., A.R.K., 1961. TERRESTRIAL PHOTOGRAMMETRY OF CLOUDS. *Journal of*
727 *Meteorology* 18, 682–687. URL: [https://doi.org/10.1175/1520-0469\(1961\)018<0682:TP0C>2.0.](https://doi.org/10.1175/1520-0469(1961)018<0682:TP0C>2.0.CO;2)
728 [CO;2](https://doi.org/10.1175/1520-0469(1961)018<0682:TP0C>2.0.CO;2), doi:10.1175/1520-0469(1961)018<0682:TP0C>2.0.CO;2.

729 Peng, Z., Yu, D., Huang, D., Heiser, J., Yoo, S., Kalb, P., 2015. 3d cloud detection and tracking system
730 for solar forecast using multiple sky imagers. *Solar Energy* 118, 496–519. URL: [http://dx.doi.org/](http://dx.doi.org/10.1145/2554850.2554913)
731 [10.1145/2554850.2554913](http://dx.doi.org/10.1145/2554850.2554913), doi:10.1145/2554850.2554913.

732 Roy, J.C.E., 2016. Design and installation of a Sky-camera network and data acquisition system for intra-
733 hour solar irradiance and photovoltaic system output forecasting. Ph.D. thesis. Murdoch University.
734 Available online: <http://researchrepository.murdoch.edu.au/id/eprint/36738/>.

735 Savoy, F.M., Dev, S., Lee, Y.H., Winkler, S., 2017. Stereoscopic cloud base reconstruction us-
736 ing high-resolution whole sky imagers , 141–145URL: [https://pdfs.semanticscholar.org/d20d/](https://pdfs.semanticscholar.org/d20d/5f1c11b3903bf07d12a94f6be8b98dbc840c.pdf)
737 [5f1c11b3903bf07d12a94f6be8b98dbc840c.pdf](https://pdfs.semanticscholar.org/d20d/5f1c11b3903bf07d12a94f6be8b98dbc840c.pdf), doi:10.1109/ICIP.2017.8296259.

738 Scaramuzza, D., Martinelli, A., Siegwart, R., 2006. A toolbox for easily calibrating omnidirectional
739 cameras, in: 2006 IEEE/RSJ International Conference on Intelligent Robots and Systems, IEEE.
740 pp. 5695–5701. URL: <http://ieeexplore.ieee.org/abstract/document/4059340/>, doi:10.1109/
741 [IROS.2006.282372](http://ieeexplore.ieee.org/abstract/document/4059340/).

742 Schmidt, M., Heller, C.M.A., Mayer, O.G., Zettl, M., Gonzalez, O.I.S., Hernandez, Y.N.M., Lynass,
743 M.R., Serra, E.B., Hartung, M., 2015. Methods and systems for predicting cloud movement. US
744 Patent 9,007,460.

745 Seiz, G., Shields, J., Feister, U., Baltsavias, E., Gruen, A., 2007. Cloud mapping with ground-based
746 photogrammetric cameras. *International Journal of Remote Sensing* 28, 2001–2032. URL: <http://dx.doi.org/10.1080/01431160600641822>, doi:10.1080/01431160600641822.

748 Singh, S., Rondinelli, M., Herman, H., 2006. System and method for panoramic imaging. US Patent
749 7,058,239.

750 Stefferud, K., Kleissl, J., Schoene, J., 2012. Solar forecasting and variability analyses using sky camera
751 cloud detection and motion vectors, in: 2012 IEEE Power and Energy Society General Meeting, pp.
752 1–6. doi:10.1109/PESGM.2012.6345434.

753 Strachey, R., Whipple, G.M., 1891. Cloud photography conducted under the Meteorological Council at
754 the Kew Observatory. *Proceedings of the Royal Society of London* 49, 467–480. URL: [http://rsp1.](http://rsp1.royalsocietypublishing.org/content/49/296-301/467.short)
755 [royalsocietypublishing.org/content/49/296-301/467.short](http://rsp1.royalsocietypublishing.org/content/49/296-301/467.short), doi:10.1098/rsp1.1890.0117,
756 [arXiv:http://rsp1.royalsocietypublishing.org/content/49/296-301/467.full.pdf+html](http://rsp1.royalsocietypublishing.org/content/49/296-301/467.full.pdf+html).

757 Tapakis, R., Charalambides, A., 2013. Equipment and methodologies for cloud detection and classifi-
758 cation: A review. *Solar Energy* 95, 392–430. URL: [http://dx.doi.org/10.1016/j.solener.2012.](http://dx.doi.org/10.1016/j.solener.2012.11.015)
759 11.015, doi:10.1016/j.solener.2012.11.015.

760 Taravat, A., Frate, F.D., Cornaro, C., Vergari, S., 2015. Neural networks and support vector machine
761 algorithms for automatic cloud classification of whole-sky ground-based images. *IEEE Geoscience*
762 *and Remote Sensing Letters* 12, 666–670. URL: <https://doi.org/10.1109/LGRS.2014.2356616>,
763 doi:10.1109/LGRS.2014.2356616.

764 Tohsing, K., Schrepf, M., Riechelmann, S., Schilke, H., Seckmeyer, G., 2013. Measuring high-resolution
765 sky luminance distributions with a CCD camera. *Appl. Opt.* 52, 1564–1573. URL: [http://ao.osa.](http://ao.osa.org/abstract.cfm?URI=ao-52-8-1564)
766 [org/abstract.cfm?URI=ao-52-8-1564](http://ao.osa.org/abstract.cfm?URI=ao-52-8-1564), doi:10.1364/AO.52.001564.

767 Tohsing, K., Schrepf, M., Riechelmann, S., Seckmeyer, G., 2014. Validation of spectral sky radiance
768 derived from all-sky camera images - a case study. *Atmospheric Measurement Techniques* 7, 2137–2146.
769 URL: <http://www.atmos-meas-tech.net/7/2137/2014/>, doi:10.5194/amt-7-2137-2014.

770 Tzoumanikas, P., Nikitidou, E., Bais, A., Kazantzidis, A., 2016. The effect of clouds on surface solar
771 irradiance, based on data from an all-sky imaging system. *Renewable Energy* 95, 314 – 322. URL: <http://www.sciencedirect.com/science/article/pii/S0960148116303305>, doi:[https://doi.org/10.](https://doi.org/10.1016/j.renene.2016.04.026)
772 [1016/j.renene.2016.04.026](https://doi.org/10.1016/j.renene.2016.04.026).

774 Urquhart, B., Chow, C.W., Nguyen, D., Kleissl, J., Sengupta, M., Blatchford, J., Jeon, D., 2012. Towards
775 intra-hour solar forecasting using two sky imagers at a large solar power plant. *Proceedings of the*
776 *American Solar Energy Society, Denver, CO, USA* URL: [https://ases.conference-services.net/](https://ases.conference-services.net/resources/252/2859/pdf/SOLAR2012_0791_full%20paper.pdf)
777 [resources/252/2859/pdf/SOLAR2012_0791_full%20paper.pdf](https://ases.conference-services.net/resources/252/2859/pdf/SOLAR2012_0791_full%20paper.pdf).

778 de WA, W., 1885. The Heights of Clouds. *Nature* 32, 630–631. URL: [http://www.nature.com/nature/](http://www.nature.com/nature/journal/v32/n835/abs/032630b0.html)
779 [journal/v32/n835/abs/032630b0.html](http://www.nature.com/nature/journal/v32/n835/abs/032630b0.html), doi:doi:10.1038/032630b0.

780 Wiegmann, D.A., Goh, J., O’Hare, D., 2002. The role of situation assessment and flight experience in
781 pilots’ decisions to continue visual flight rules flight into adverse weather. *Human Factors* 44, 189–
782 197. URL: <https://doi.org/10.1518/0018720024497871>, doi:10.1518/0018720024497871. PMID:
783 12452267.

784 Xia, M., Lu, W., Yang, J., Ma, Y., Yao, W., Zheng, Z., 2015. A hybrid method based on extreme
785 learning machine and k-nearest neighbor for cloud classification of ground-based visible cloud image.
786 *Neurocomputing* 160, 238 – 249. URL: [http://www.sciencedirect.com/science/article/pii/](http://www.sciencedirect.com/science/article/pii/S092523121500171X)
787 [S092523121500171X](http://www.sciencedirect.com/science/article/pii/S092523121500171X), doi:<https://doi.org/10.1016/j.neucom.2015.02.022>.